
Angular clustering and host halo properties of [OII] emitters at $z > 1$ in the Subaru HSC survey

Teppei OKUMURA,^{1,2*} Masao HAYASHI,³ I-Non CHIU,¹ Yen-Ting LIN,¹
Ken OSATO,⁴ Bau-Ching HSIEH,¹ and Sheng-Chieh LIN^{1,5}

¹Institute of Astronomy and Astrophysics, Academia Sinica, No. 1, Section 4, Roosevelt Road, Taipei 10617, Taiwan

²Kavli Institute for the Physics and Mathematics of the Universe (WPI), UTIAS, The University of Tokyo, Kashiwa, Chiba 277-8583, Japan

³National Astronomical Observatory, Mitaka, Tokyo 181-8588, Japan

⁴Institut d'Astrophysique de Paris, Sorbonne Université, CNRS, UMR 7095, 75014 Paris, France

⁵Department of Physics and Astronomy, University of Kentucky, 505 Rose Street, Lexington, KY 40506, USA.

*E-mail: tokumura@asiaa.sinica.edu.tw

Received 2020 December 23; Accepted 2021 June 11

Abstract

We study the angular correlation function of star-forming galaxies and properties of their host dark matter halos at $z > 1$ using the Hyper-Suprime Cam (HSC) Subaru Strategic Program (SSP) survey. We use [OII] emitters identified using two narrow-band (NB) filters, *NB816* and *NB921*, in the Deep/UltraDeep layers, which respectively cover large angular areas of 16.3 deg^2 and 16.9 deg^2 . Our sample contains 8302 and 9578 [OII] emitters at $z = 1.19$ (*NB816*) and $z = 1.47$ (*NB921*), respectively. We detect a strong clustering signal over a wide angular range, $0.001 < \theta < 1$ [deg], with the bias $b = 1.61^{+0.13}_{-0.11}$ ($z = 1.19$) and $b = 2.09^{+0.17}_{-0.15}$ ($z = 1.47$). We also find a clear deviation of the correlation from a simple power-law form. To interpret the measured clustering signal, we adopt a halo occupation distribution (HOD) model that is constructed to explain the spatial distribution of galaxies selected by a star formation rate. The observed correlation function and number density are simultaneously explained by the best-fitting HOD model. From the constrained HOD model, the average mass of halos hosting the [OII] emitters is derived to be $\log M_{\text{eff}}/(h^{-1}M_{\odot}) = 12.70^{+0.09}_{-0.07}$ and $12.61^{+0.09}_{-0.05}$ at $z = 1.19$ and 1.47 , respectively, which will become halos with the present-day mass, $M \sim 1.5 \times 10^{13} h^{-1} M_{\odot}$. The satellite fraction of the [OII] emitter sample is found to be $f_{\text{sat}} \sim 0.15$. All these values are consistent with the previous studies of similar samples, but we obtain tighter constraints even in a larger parameter space due to the larger sample size from the HSC. The results obtained for host halos of [OII] emitters in this paper enable the construction of mock galaxy catalogs and the systematic forecast study of cosmological constraints from upcoming emission line galaxy surveys such as the Subaru Prime Focus Spectrograph survey.

Key words: cosmology: observations — galaxies: formation — galaxies: halos — large-scale structure of universe — methods: statistical

1 Introduction

Observation of the large-scale structure of the Universe via the distribution of galaxies in galaxy redshift surveys provides a powerful tool to reveal the nature of dark matter and dark energy (Peebles 1980; Weinberg et al. 2013). As dark energy started to become a dominant energy component toward today, the Universe experienced a transition from decelerating to accelerating expansion at redshift around unity. It is thus crucial to investigate the large-scale spatial distribution of galaxies over a broad redshift range from $z = 0$ to $z > 1$.

The relation between galaxies and their host dark matter halos has been extensively investigated using the prescription of the halo occupation distribution (HOD) modeling (Jing et al. 1998; Seljak 2000; Peacock & Smith 2000; Ma & Fry 2000; Scoccimarro et al. 2001; Berlind & Weinberg 2002; Cooray & Sheth 2002). Galaxies selected by the colors, specific star formation rates (sSFR), and stellar masses, have been mainly used as tracers of the large-scale structure in wide-angle galaxy redshift surveys. There are a lot of preceding studies of the HOD modeling for such populations, and it is known that a simple model proposed by Zheng et al. (2005) can describe the spatial distribution of these galaxies (e.g., Zehavi et al. 2005; Blake et al. 2008; Zheng et al. 2009; Abbas et al. 2010; Zehavi et al. 2011; White et al. 2011; Wake et al. 2011; Coupon et al. 2012; de la Torre et al. 2013; Reid et al. 2014; Guo et al. 2014; Koda et al. 2016; Ishikawa et al. 2020). Most of the work is, however, limited at redshift less than unity because these types of galaxies become harder to target at higher redshifts (Takada et al. 2014; DESI Collaboration et al. 2016): for early/red-type galaxies one needs long exposure time to get the 4000\AA break and for color-selected galaxies the accuracy of the photometric redshift becomes worse at such redshifts. On the other hand, statistical properties of dark matter halos have been studied using the HOD of high- z quasars and galaxies, i.e., Lyman-break galaxies or Lyman- α emitters at $z > 2$, for relatively narrow angular regions (Bullock et al. 2002; Moustakas & Somerville 2002; Hamana et al. 2004; Conroy et al. 2006; Richardson et al. 2012; Kayo & Oguri 2012; Durkalec et al. 2015; Harikane et al. 2016; Ishikawa et al. 2017; Harikane et al. 2018).

Due to the observational limit of color/sSFR/stellar mass-selected galaxies at higher redshifts, recently the focus of large galaxy surveys has turned to emission line galaxies (ELGs) that can be targeted at $z > 1$. Such surveys include the Subaru FastSound survey (Tonegawa et al. 2015; Okada et al. 2016), extended Baryon Oscillation Spectroscopic Survey (eBOSS: Dawson et al. 2016), the Hobby-Eberly Telescope Dark Energy Experiment (HETDEX: Adams et al. 2011), Subaru Prime Focus Spectrograph (PFS: Takada et al. 2014), Dark Energy Spectroscopic Instrument (DESI: DESI Collaboration et al.

2016), the Spectro-Photometer for the History of the Universe, Epoch of Reionization, and Ices Explorer (SPHEREx: Doré et al. 2014), and *Euclid* (Laureijs et al. 2011). However, statistical properties of the host halos for ELGs are not as simple as those for galaxies selected by colors, sSFR and stellar masses because unlike them there does not necessarily exist an ELG in the center of a halo at the massive end. Geach et al. (2012) proposed a model of HOD for ELGs taking into account the fact that ELGs selected via star formation rates do not necessarily reside in the centers of massive halos. Then they placed a constraint on the HOD parameters for $H\alpha$ emitters from the Hi-Z Emission Line Survey (HiZELS: Geach et al. 2008). The HOD of the HiZELS sample has been reanalyzed by Cochrane et al. (2017) and Cochrane et al. (2018). Although a simple HOD modeling has been performed for $H\alpha$ emitters of the FastSound survey at $z \sim 1.4$ in Okumura et al. (2016), the sample was so sparse that the clustering signal has been consistent with the HOD of central galaxies only. Kashino et al. (2017) analyzed the $H\alpha$ -selected galaxies from the FMOS-COSMOS survey at $z \sim 1.6$ and constrained the HOD model, but they still adopted the simple model of Zheng et al. (2005). The detailed HOD modeling has been performed by Hong et al. (2019) for $Ly\alpha$ emitters at $z \sim 2.67$ selected from the NOAO Deep Wide-Field Survey.

Since [OII] emitters ($\lambda = 3726, 3729 \text{\AA}$) are one of the main tracers of the large-scale structure employed in upcoming cosmological surveys, it is of crucial importance to investigate properties of halos which host them. So far, however, there are few observational studies of the HOD modeling for [OII] emitters. From the HiZELS survey Khostovan et al. (2018) measured the clustering of $H\beta + [\text{OIII}]$ as well as [OII] emitters, but they did not find deviation of the correlation function from a power-law form. Rather than the HOD, properties of [OII] emitters have been investigated using a semi-analytic model of galaxy formation (e.g., Contreras et al. 2013; Gonzalez-Perez et al. 2018; Favole et al. 2020; Gonzalez-Perez et al. 2020; Avila et al. 2020). Guo et al. (2019) analyzed the clustering of spectroscopically-identified [OII] emitting galaxies at $0.7 < z < 1.2$ from the eBOSS survey. They then investigated properties of the host halos using the conditional stellar mass function. Recently there are also attempts to determine the HOD of ELGs by directly identifying emission lines in cosmological hydrodynamical simulations (Hadzhiyska et al. 2020; Osato & Okumura 2021). Properties of the luminosity function of [OII] and other ELGs are also being actively investigated (e.g., Comparat et al. 2016; Saito et al. 2020; Hayashi et al. 2020; Gao & Jing 2020).

In this paper we present a detailed HOD modeling for [OII] emitters identified by Narrow-Band (NB) filters in the Subaru Hyper-Suprime Cam (HSC) survey. NB imaging surveys of ELGs allow us to cover a wide and homogeneous field of view.

Table 1. Summary of the [OII] ELG data used in this paper.*

Field	<i>NB816</i> ($1.178 < z < 1.208$)				<i>NB921</i> ($1.453 < z < 1.489$)			
	Area (deg ²)	N_g	$n_g (h^3 \text{Mpc}^{-3})$	N_{sub}	Area (deg ²)	N_g	$n_g (h^3 \text{Mpc}^{-3})$	N_{sub}
COSMOS	1.37	566	4.48×10^{-3}	9	5.80	3134	4.30×10^{-3}	41
DEEP2-3	4.98	2485	5.40×10^{-3}	35	4.92	2107	3.41×10^{-3}	35
ELAIS-N1	4.81	2927	6.59×10^{-3}	34	4.81	3098	5.13×10^{-3}	34
SXDS+XMM-LSS	5.17	2324	4.86×10^{-3}	37	1.33	1239	7.44×10^{-3}	9
Total	16.33	8302	5.50×10^{-3}	115	16.86	9578	4.53×10^{-3}	119

* The value of the area shows the one after masking with bright object masks, N_g is the number of the galaxies used in this paper after making the magnitude and flux cuts, n_g is the number densities of the galaxies, and N_{sub} is the number of sub-regions using jackknife resampling (see section 3.2). The last row shows the values for the sum of the four fields.

Thus it provides a suitable sample to probe the large-scale spatial distribution of emission-line galaxies. We, for the first time, constrain the general HOD model proposed by Geach et al. (2012) for populations of [OII] emitters at $z = 1.19$ and $z = 1.47$ in the HSC survey. We then discuss properties of dark matter halos which host the [OII] emitters based on the constrained HOD parameters.

The structure of this paper is as follows. Section 2 describes the HSC survey and the [OII] emitter sample. Section 3 presents the measurements of the angular correlation function and its covariance matrix. Power-law and linearly-biased dark matter model fittings are shown in section 4. We also discuss dependences of the correlation function amplitude on different stellar mass and emission line luminosity thresholds. The detailed HOD modeling is performed for the measured correlation functions in section 5. Conclusions are given in section 6. We compare the angular correlation functions measured from four individual fields in appendix 1. We present the HOD parameter constraints without using the information of the measured abundance of [OII] emitters in appendix 2.

Throughout this paper, we assume a flat Λ CDM cosmology with the cosmological parameters based on the results of Planck CMB measurements (Planck Collaboration et al. 2016): $\Omega_m = 1 - \Omega_\Lambda = 0.307$, $\Omega_b = 0.0486$, $h = 0.677$, $n_s = 0.967$ and $\sigma_8 = 0.816$.

2 Data

2.1 Hyper-Suprime Cam Survey

The HSC Subaru Strategic Program (SSP) is an ongoing imaging survey since 2014 (Aihara et al. 2018b) with a 1.77 deg^2 field-of-view imaging camera installed on the Subaru Telescope (Miyazaki et al. 2012; Miyazaki et al. 2018; Furusawa et al. 2018; Komiyama et al. 2018).

In the HSC survey the deep imaging is conducted in five broad-band (BB) filters as well as four Narrow-Band (NB) filters in the Deep (D) and UltraDeep (UD) layers over 28 deg^2 in total. The imaging reduction and catalog construction are car-

ried out by Bosch et al. (2018) and Huang et al. (2018). In 2019, the second public data release (PDR2) of the HSC SSP data has been made (Aihara et al. 2019).

2.2 Narrow Band filters and [OII] emitter sample

We use the data from two NB filters, *NB816* and *NB921*, constructed by Hayashi et al. (2020) based on the D and UD layers of Subaru-SSP from the PDR2. These data are significantly updated from the version of PDR1 (Aihara et al. 2018a; Hayashi et al. 2018). The coverage of *NB816* and *NB921* increases to 26 deg^2 covered by 13 pointings and 28 deg^2 covered by 14 pointings, respectively, from the PDR1 (Aihara et al. 2019). We apply the bright star masks modified from Coupon et al. (2018) and Aihara et al. (2019) because Hayashi et al. (2020) noticed that the mask size for some bright stars is not large enough to remove false detections around prominent stellar halos. As a result, the total area is reduced to 16.3 deg^2 (*NB816*) and 16.9 deg^2 (*NB921*), as shown in table 1.

The survey area in the D layer, where the NB data are available, consists of four separate fields: E-COSMOS, DEEP2-3, ELAIS-N1, and XMM-LSS. Furthermore, each of E-COSMOS and XMM-LSS fields encompasses the UD layer covered by a single pointing of HSC, named UD-COSMOS and SXDS, respectively. Since UD-COSMOS and E-COSMOS are jointly processed, we call the combination the COSMOS field.

The complete description of the [OII] emitter sample used in this study is provided in Hayashi et al. (2018) and Hayashi et al. (2020). While we briefly summarize our sample in the following, we refer the reader to these papers for more details. The ELGs are selected using the NB data together with data from the five BB filters. [OII] emitters are observed by *NB816* and *NB921* filters in two narrow redshift ranges, $1.178 < z < 1.208$ and $1.453 < z < 1.489$, respectively. To identify the [OII] emitters, we use spectroscopic redshifts if available and photometric redshifts otherwise. If a galaxy has a spectroscopic redshift outside of the ranges above, we remove it as a contaminant. When the photometric redshift is used, we have taken into account its

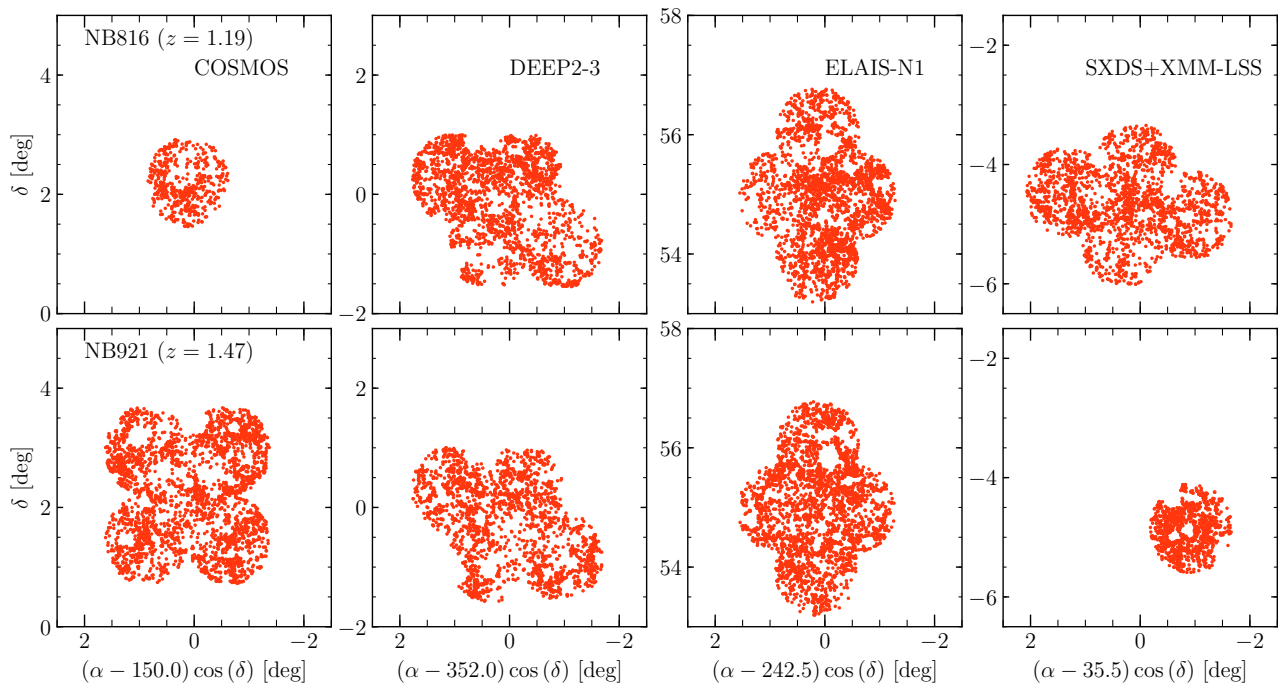


Fig. 1. Angular distribution of [OII] emitters at $z = 1.19$ (top) and $z = 1.47$ (bottom) with line flux greater than $3 \times 10^{-17} \text{ erg s}^{-1} \text{ cm}^{-2}$ and magnitude brighter than 23.5 mag in the NB filters, *NB816* and *NB921*, respectively, for the individual four fields. The large empty areas where no galaxy is found are mostly the regions masked for bright objects. See figure 4 of Hayashi et al. (2020) for details of the mask information.

uncertainty for the identification of [OII] emitters. For galaxies not identified with spectroscopic or photometric redshifts, we use the color-color diagrams to distinguish [OII] emitters from other possibilities. Galaxies selected as NB [OII] emitters are expected to be star-forming galaxies (Ly et al. 2012; Hayashi et al. 2013). Thus, our sample is limited by star forming rate (SFR). While our [OII] emission lines are affected by the dust extinction, the majority of typical star-forming galaxies is properly selected because the cosmic SFR density in our catalogs is consistent with other preceding studies (Hayashi et al. 2020).

We make magnitude and flux cuts on our data, the model magnitude¹ $m \leq 23.5$ and the estimated line flux of $\geq 3 \times 10^{-17} \text{ erg s}^{-1} \text{ cm}^{-2}$. We refer the reader to Hayashi et al. (2020) for the details of the line flux estimation. The limiting magnitude of the NB filters is much deeper than 23.5 [mag] so that fainter [OII] emitters have been included in our sample, and accordingly [OII] emitters which have the line flux with $(1 - 2) \times 10^{-17} \text{ erg s}^{-1} \text{ cm}^{-2}$ have been selected. However, we have made such conservative magnitude and flux cuts to assure the completeness of the sample. With these ranges, the number density indeed increases monotonically with decreasing the flux or increasing the magnitude (see Hayashi et al. 2018; Hayashi et al. 2020) and the mean completeness of our [OII] sample becomes 0.974 for *NB816* and 0.956 for *NB921*. The numbers of [OII] emitters are then reduced to 8302 and

9578 for *NB816* and *NB921* data, respectively. See table 1 for the numbers of the sample for each field. The line flux cut corresponds to the observed line luminosity thresholds of $L \geq 2.56 \times 10^{41} [\text{erg s}^{-1}]$ ($z = 1.19$) and $L \geq 4.30 \times 10^{41} [\text{erg s}^{-1}]$ ($z = 1.47$). The median luminosity with the 2.5th–97.5th percentiles is $\bar{L} = 4.49^{+12.67}_{-1.82} \times 10^{41} [\text{erg s}^{-1}]$ at $z = 1.19$ and $\bar{L} = 7.88^{+16.95}_{-3.35} \times 10^{41} [\text{erg s}^{-1}]$ at $z = 1.47$. Stellar masses for the [OII] emitters are estimated by spectral energy distribution fit with five HSC BB data in Hayashi et al. (2020). The median stellar mass of our [OII] emitter sample with the 2.5th–97.5th percentiles is $\bar{M}_* = 8.58^{+132.54}_{-7.13} \times 10^9 M_\odot$ at $z = 1.19$ and $\bar{M}_* = 1.72^{+12.40}_{-1.41} \times 10^{10} M_\odot$ at $z = 1.47$.

Not all the galaxies in the catalog are real [OII] emitters, but some are fake lines due to noise and some others are real emission lines but not [OII] emitters. The contamination rate is investigated by applying the photo- z and color selections to galaxies confirmed with spectroscopic redshifts. The fraction of such non-[OII] emitters has been significantly reduced in the current sample compared to that in the PDR1 catalog because (1) the method of selecting emission-line galaxies has been improved from using the `cmode1` magnitude to the fixed aperture magnitude (Hayashi et al. 2020) and (2) the pipeline used for the data process, `hscPipe`, has been upgraded in the PDR2 (Bosch et al. 2018; Aihara et al. 2019). The analysis by Hayashi et al. (2020) estimated the fraction of non-[OII] emitters in our sample is less than 10% for most cases and $\sim 20\%$ at most, by

¹ We use a composite model magnitude named `cmode1`.

applying photometric redshift and color selections to galaxies confirmed with spectroscopic redshifts. This contaminant fraction can be further reduced by a machine-learning based technique for photometric redshift estimates (see e.g., Hsieh & Yee 2014). However, since the current contaminant fraction is low enough for our analysis, we do not include this process. The angular distribution of the [OII] emitters is shown in figure 1. Table 1 summarizes the properties of the data.

2.3 Random catalog

The HSC-SSP PDR2 provides us with the catalog of random points across the survey area as one of the value-added products (see subsection 5.4 of Aihara et al. 2019). The number density of the random points is 100 per square arcmin. We apply the same basic flags as those for the emission-line galaxies except for the flags related to the source detection (i.e., `merge_peak`, `sdsshape_flag`, `cmodel`, and `psfflux`) to select the random points (see subsection 2.1.1 of Hayashi et al. 2020). We also apply the same bright star masks as those used for the selection of the emission-line galaxies to the random points (see Hayashi et al. 2020 for the details of the masks and also subsection 6.6.2 of Aihara et al. 2019, as well as Coupon et al. 2018). Consequently, the random points used in this study are distributed over the regions identical to where the emission-line galaxies are surveyed.

3 Angular correlation function

In this paper we analyze the spatial distribution of [OII] emitters using the angular correlation function. The angular correlation function is related to the spatial correlation function in three dimension through the relation (Peebles 1973; Peebles 1980):

$$w(\theta) = \int dx_1 p(x_1) \int dx_2 p(x_2) \xi(r), \quad (1)$$

where r is the 3-d separation between two galaxies, $r = [x_1^2 + x_2^2 - 2x_1x_2 \cos \theta]^{1/2}$, $x_i = x(z_i)$ is the comoving distance to a galaxy at redshift z_i , and $p(x)$ is the radial selection function normalized as $\int_0^\infty dx p(x) = 1$.

3.1 Correlation function estimation

We first measure the angular correlation function of [OII] emitters at $z = 1.19$ and $z = 1.47$ from the four fields, COSMOS, DEEP2-3, ELAIS-N1, and SXDS+XMM-LSS. We then combine the four correlation functions at each redshift for the statistical analysis.

We adopt the Landy-Szalay estimator (Landy & Szalay 1993) to measure the angular correlation function,

$$\hat{w}_k(\theta) = \frac{DD_k - 2DR_k - RR_k}{RR_k}, \quad (2)$$

where DD_k , RR_k , and DR_k are respectively the normalized counts of data-data, random-random, and data-random pairs at given angular separation θ . The random catalogs contain large numbers of points, which are more than 600 times as dense as our [OII] emitter catalogs to ensure that the shot noise due to the finite random points is negligible. The subscript k denotes the k th field ($1 \leq k \leq 4$) and hat means an estimated quantity which can be different from the true one [see equation (6) below]. To combine the correlation function measurements from the four fields, we weigh each measurement by a function W_k ,

$$1 + \hat{w}(\theta) = \frac{\sum_{k=1}^4 W_k^2(\theta) (1 + \hat{w}_k(\theta))}{\sum_{k=1}^4 W_k^2(\theta)}. \quad (3)$$

Thus the combined correlation function is expressed as

$$\hat{w}(\theta) = \frac{\sum_{k=1}^4 W_k^2(\theta) \hat{w}_k(\theta)}{\sum_{k=1}^4 W_k^2(\theta)}. \quad (4)$$

We adopt the inverse-variance weighting, $W_k(\theta) = \sigma_k^{-1}(\theta)$, where $\sigma_k^2(\theta)$ is the diagonal component of the covariance matrix in the k -th field (see next subsection).

The correlation function measured above is underestimated by a constant due to the finite survey area. The effect is known as the integral constraint (Peebles & Groth 1976) and calculated as

$$w_\Omega = \frac{1}{\Omega} \int_\Omega d\Omega_1 d\Omega_2 w(\theta), \quad (5)$$

where the integral is performed over the solid angle of the survey, Ω . The integral constraint is calculated by a given model of the correlation function $w(\theta; \Theta)$, where Θ is a set of model parameters (see sections 4 and 5). Note also that the clustering amplitude is further reduced compared to the true clustering of [OII] emitters due to the contamination of non-[OII] emitters and noise lines. As seen in section 4, we assume that the correlation of non-[OII] emitters is negligible. Then the estimated correlation function is related to the true correlation function w as

$$\hat{w}(\theta) = (1 - f_{\text{fake}})^2 (w(\theta) - w_\Omega), \quad (6)$$

where f_{fake} is the fraction of non-[OII] emitters in our sample, $0.1 \lesssim f_{\text{fake}} \lesssim 0.2$ (see section 2.2).

The measured correlation function, combined over the four fields, \hat{w} , is shown as the red points in the upper and lower panels of Figure 2 for $z = 1.19$ and $z = 1.47$, respectively. The correlation function becomes negative at scales, $\theta \sim 1$ deg ($r \sim 50h^{-1}$ Mpc), due to the integral constraint w_Ω . For the model parameter fitting below, this effect is properly taken into account. In this figure we show various lines, which are the predictions based on the power-law model and the linearly-biased dark matter model. We discuss these in detail in section 4. The measurements of the angular correlation functions for individual fields are presented for a consistency check in appendix 1.

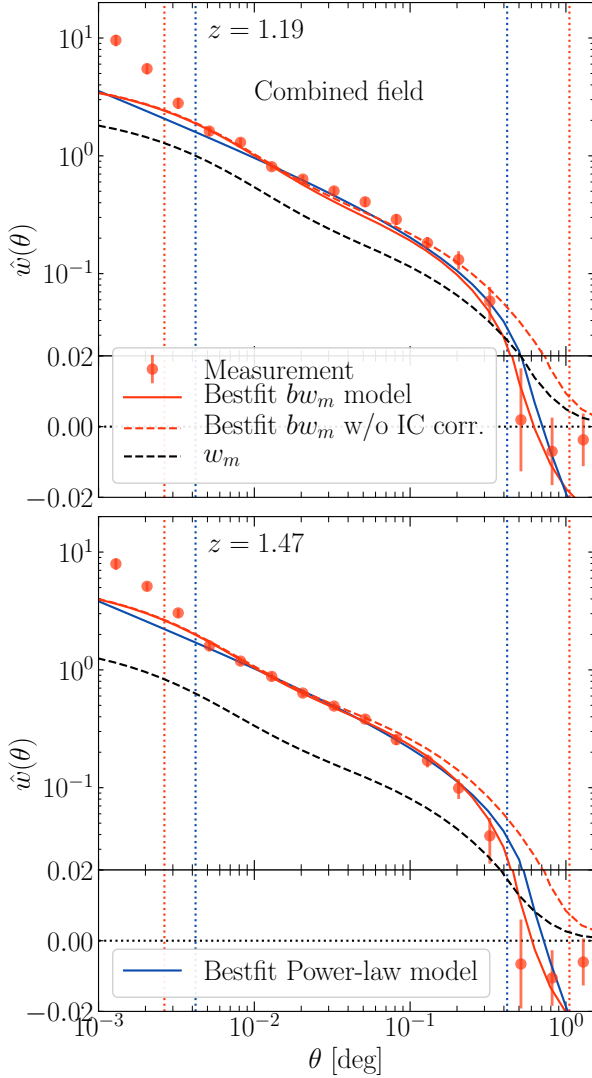


Fig. 2. Angular correlation functions of [OII] emitters measured from the entire four fields at $z = 1.19$ (top) and $z = 1.47$ (bottom). Note that the vertical axis mixes logarithmic and linear scalings. The red points are the measurement without the integral constraint correction, \hat{w} . The errorbars are estimated from jackknife resampling. The blue solid curve is the best-fitting model of the power-law model, $(1 - f_{\text{fake}})^2(w(\theta; A_w, \beta) - w_\Omega(A_w, \beta))$, with $(A_w, \beta, f_{\text{fake}}) = (1.10, 0.534, 0.140)$ for $z = 1.19$ and $(1.17, 0.538, 0.139)$ for $z = 1.47$. The data enclosed by the two blue vertical lines are used for this analysis. The red solid curve is the best-fitting model of the linearly-biased dark matter model, $(1 - f_{\text{fake}})^2(b^2 w_m(\theta) - w_\Omega(b))$, with $(b, f_{\text{fake}}) = (1.60, 0.140)$ for $z = 1.19$ and $(2.08, 0.140)$ for $z = 1.47$ when the data enclosed by the two red vertical lines are used. The red dashed curve is the same model but without subtracting the integral constraint denoted by IC in the legend, $(1 - f_{\text{fake}})^2 b^2 w_m(\theta)$. The non-linear dark matter correlation function, $w_m(\theta)$, is shown by the red dashed curve as a reference.

3.2 Covariance matrix

We use the Jackknife resampling technique to estimate the covariance error matrix (see, e.g., Lupton 1993). The covariance of the angular correlation function for k -th field, $C_{k,ij} \equiv C(\hat{w}_k(\theta_i), \hat{w}_k(\theta_j))$, is then estimated as

$$C_{k,ij} = \frac{N_{\text{sub}} - 1}{N_{\text{sub}}} \times \sum_{\ell=1}^{N_{\text{sub}}} (\hat{w}_k^\ell(\theta_i) - \bar{w}_k(\theta_i)) (\hat{w}_k^\ell(\theta_j) - \bar{w}_k(\theta_j)), \quad (7)$$

where $\hat{w}_k^\ell(\theta_i)$ is the correlation function in the i -th angular bin in ℓ -th jackknifed realization, N_{sub} is the number of realizations in the k -th field and $\bar{w}_k(\theta_i) = N_{\text{sub}}^{-1} \sum_{\ell=1}^{N_{\text{sub}}} \hat{w}_k^\ell(\theta_i)$. The values of N_{sub} for each field are shown in table 1. In total, we use 115 and 119 jackknifed realizations for the $z = 1.19$ and 1.47 data, respectively. We use the k -means algorithm² to divide our survey regions to subregions with the same angular areas. Each subsample includes a region continuous on the sky, 0.38 deg on a side, which corresponds to the comoving size of $17h^{-1}\text{Mpc}$ at $z = 1.19$ and $20h^{-1}\text{Mpc}$ at $z = 1.47$. Just like equation (4), the covariance matrixes from the four fields can be combined to $C_{ij} \equiv C(w(\theta_i), w(\theta_j))$ as

$$C_{ij} = \frac{\sum_{k=1}^4 W_k^2(\theta_i) W_k^2(\theta_j) C_{k,ij}}{\sum_{k=1}^4 W_k^2(\theta_i) \sum_{k=1}^4 W_k^2(\theta_j)}. \quad (8)$$

The square roots of the diagonal components of the covariance matrix, $C_{ii}^{1/2}$, are shown as the error bars in figure 2.

4 Results

4.1 Setup

In this section we consider two simple models for the angular correlation function, the power-law and linearly biased dark matter models in sections 4.2 and 4.3, to model the clustering amplitude of [OII] emitters. The HOD modeling is performed in section 5.

We adopt the small-angle approximation, known as the Limber's approximation (Limber 1954; Peebles 1980). With this, the relation between the angular and spatial correlation functions given by equation (1) can be simplified to:

$$w(\theta) = 2 \int_0^\infty dx p^2(x) \int_0^\infty dh \xi(r = \sqrt{x^2 \theta^2 + h^2}), \quad (9)$$

where $x = (x_1 + x_2)/2$ and $h = x_2 - x_1$. The validity of the Limber's approximation for the angular correlation with large angle separations has been extensively discussed by, e.g., Simon (2007) and Crocce et al. (2011). The approximation breaks down on large scales when the width of the redshift distribution, $z_{\text{min}} \leq z \leq z_{\text{max}}$, is too narrow. The width of our NB filters is $\Delta x \equiv x_{\text{max}} - x_{\text{min}} \simeq 50h^{-1}\text{Mpc}$, where $x_{\text{min}} = x(z_{\text{min}})$ and

² <https://github.com/esheldon/kmeans.radec>

$x_{\max} = x(z_{\max})$, and our analysis focuses on the angular scales of $\theta < 1$ deg. We thus can safely rely on this approximation.

Although determination of the true radial selection function is not straightforward, it is known to have a form similar with the transmission curve to some extent (see, e.g., figure 3 of Hayashi et al. 2015). However, the width $\Delta x \simeq 50h^{-1}\text{Mpc}$ is narrow enough that we can simply assume the radial selection function to be a constant,

$$p(x) = \begin{cases} 1/\Delta x & \text{for } x_{\min} \leq x \leq x_{\max}, \\ 0 & \text{otherwise.} \end{cases} \quad (10)$$

Using the transmission curves available for the NB filters³, we test the effect of choices of $p(z)$ on the calculation of the angular correlation functions. We compare the angular correlation function computed using $p(z)$ from the transmission curve with that from the constant $p(z)$ in equation (10). We then find that the correlation functions $w(\theta)$ have exactly the same shape with the amplitude different by $\leq 7\%$ for both *NB816* and *NB921*. Thus, constraints on the parameters for the correlation function are not affected by the choice of $p(z)$ but it changes only the normalization, f_{fake} , by at most 4%, much smaller than our $1 - \sigma$ prior on f_{fake} , $\sim 40\%$ (see the following paragraphs of this subsection). In the following analysis, we thus adopt the simple constant radial selection function [equation (10)].

Given a model for the correlation function with a set of parameters Θ , $w(\theta; \Theta)$, the integral constraint [equation (5)] can be estimated as

$$w_{\Omega}(\Theta) = \frac{\sum_i w(\theta_i; \Theta) RR(\theta_i)}{\sum_i RR(\theta_i)}, \quad (11)$$

where θ_i is the i th separation bin and the sum is calculated over the entire bins. The normalized random-random pair count for the combined field, RR , is computed in the same way as the correlation function in equation (4),

$$RR(\theta) = \frac{\sum_{k=1}^4 W_k^2(\theta) RR_k(\theta)}{\sum_{k=1}^4 W_k^2(\theta)}. \quad (12)$$

As discussed in section 2.2, not all the lines detected as [OII] emitters are actually [OII] lines, but some are other emission lines or just noises. The fraction of fake [OII] lines is denoted as f_{fake} . Then the observed correlation function has contributions not only from the auto-correlation of [OII] emitters but also from the auto-correlation of fake lines and their cross-correlation, which are suppressed by factors of f_{fake}^2 and $2f_{\text{fake}}(1 - f_{\text{fake}})$, respectively (see e.g., van den Bosch et al. 2013; Okumura et al. 2015; Okumura et al. 2017 for detailed theoretical schemes for the tracer decomposition). The contamination fraction is estimated to be around $f_{\text{fake}} \sim 0.14$ by applying photometric redshift and color selections to galaxies confirmed with spectroscopic redshifts (Hayashi et al. 2020). Thus, even though the non-[OII] emitters have a non-negligible

auto-correlation, the (intrinsically small) clustering amplitude is suppressed by $0.14^2 \sim 0.02$. We therefore can safely assume that the observed correlation is dominated by the auto correlation of [OII] emitters (see, e.g., Okumura et al. 2016; Kashino et al. 2017 for a similar treatment)⁴. The amplitude of the correlation function is thus simply scaled by a factor of $(1 - f_{\text{fake}})^2$. We treat f_{fake} as a free parameter with a prior of $f_{\text{fake}} = 0.140 \pm 0.060$ to cover the uncertainties described in section 2.2 within the $1 - \sigma$ confidence level. We chose this uncertainty to be very conservative and much larger than it is to avoid inducing biased constraints on model parameters by imposing strong (and possibly incorrect) priors. The imposed prior is coincidentally equivalent to that adopted in Kashino et al. (2017).

Finally, once the model with parameters for the correlation function is given as $w(\theta; \Theta)$, the theoretical prediction to be compared to the observed correlation function, \hat{w} , is obtained with an additional parameter f_{fake} through equation (6). To constrain model parameters, the χ^2 statistic is calculated for the correlation function, w , as

$$\chi_w^2(\Theta) = \sum_{i=1}^{N_{\text{bin}}} \sum_{j=1}^{N_{\text{bin}}} \Delta_i C_{ij}^{-1} \Delta_j, \quad (13)$$

where N_{bin} is the number of angular separation bins used in the analysis, $\Delta_i = \hat{w}_{\text{obs}}(\theta_i) - \hat{w}_{\text{th}}(\theta_i; \Theta)$ is the difference between the observed correlation function [equation (4)] and the theoretical prediction [equation (6)] with Θ being a set of parameters to be constrained, and C_{ij}^{-1} is the inverse covariance matrix [equation (8)] multiplied by a correction for the finite realization effect, $(N_{\text{sub}} - N_{\text{bin}} - 2)(N_{\text{sub}} - 1)^{-1}$ (Hartlap et al. 2007).

In order to perform a maximum likelihood analysis, we use the Markov chain Monte Carlo (MCMC) sampler *emcee* (Foreman-Mackey et al. 2013).

4.2 Power-law constraints

It has been known that shapes of the spatial and angular correlation functions approximately follow a power law, originally found by Totsuji & Kihara (1969) (see also Peebles 1980), as

$$w(\theta; A_w, \beta) = A_w \left(\frac{\theta}{1 \text{ arcmin}} \right)^{-\beta}. \quad (14)$$

The χ^2 statistic is calculated with $\Theta = (A_w, \beta, f_{\text{fake}})$. Because a power-law model is known to fail to fit an observed correlation function at small- and large-scale limits, we compute the χ^2 statistic for a relatively narrow angular separation range, $0.004 < \theta < 0.4$ [deg], denoted by the blue vertical lines in figure 2. Thus the number of bins is $N_{\text{bin}} = 10$.

⁴ If f_{fake} becomes large so that the contribution from non-[OII] emitters is non-negligible, a sophisticated treatment of the line contaminant for the cosmological analysis is required (e.g., Leung et al. 2017; Addison et al. 2019).

³ <https://subarutelescope.org/Observing/Instruments/HSC/sensitivity.html>

Table 2. Parameter constraints on single power-law and linearly-biased dark matter models*

Power-law parameter	Prior	NB816		NB921	
		Best-fit	Posterior PDF	Best-fit	Posterior PDF
A_w (at 1 arcmin)	None	1.10	$1.12^{+0.21}_{-0.16}$	1.17	$1.20^{+0.20}_{-0.17}$
β	None	0.534	$0.533^{+0.057}_{-0.055}$	0.538	$0.537^{+0.044}_{-0.043}$
f_{fake}	0.140 ± 0.060	0.140	$0.149^{+0.059}_{-0.059}$	0.139	$0.149^{+0.060}_{-0.059}$
r_0 ($h^{-1}\text{Mpc}$)	–	4.08	$4.12^{+0.50}_{-0.41}$	4.55	$4.61^{+0.51}_{-0.45}$
Linearly-biased DM Parameter	Prior	Best-fit	Posterior PDF	Best-fit	Posterior PDF
b	None	1.60	$1.61^{+0.13}_{-0.11}$	2.08	$2.09^{+0.17}_{-0.15}$
f_{fake}	0.140 ± 0.060	0.140	$0.145^{+0.059}_{-0.059}$	0.140	$0.145^{+0.060}_{-0.059}$

* The values in the column of ‘‘Prior’’ quote the mean and standard deviation of the Gaussian priors. The column of ‘‘Best-fit’’ shows the parameter set which gives the minimum value of χ^2 . In the column of ‘‘Posterior PDF’’, the central value is a median and the error means 16 – 84 percentiles after other parameters are marginalized over.

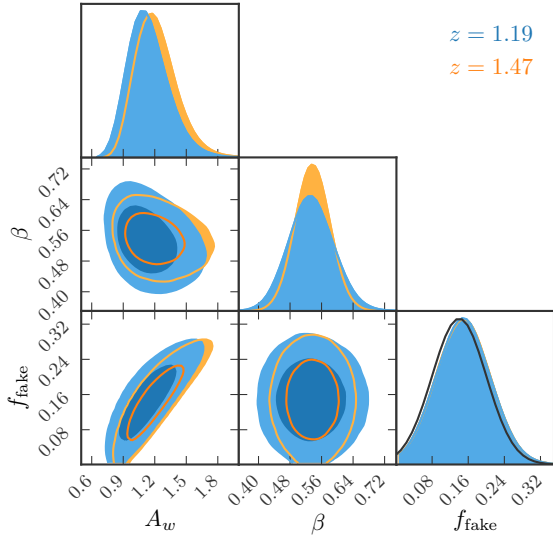


Fig. 3. Constraints on the power-law model parameters (A_w, β) and the fake line fraction parameter f_{fake} from the angular clustering of [OII] emitters for $z = 1.19$ (blue) and $z = 1.47$ (orange). Contours show the 68% and 95% confidence levels. The diagonal panel show the posterior probability distribution of each parameter. A Gaussian prior is adopted for the fake line fraction, $f_{\text{fake}} = 0.140 \pm 0.060$, which is shown as the black curve compared with the one-dimensional posterior. The posterior of f_{fake} for $z = 1.47$ (orange) is almost entirely behind the one for $z = 1.19$.

Figure 3 shows the joint constraints on the power-law parameters and the fake line fraction, ($A_w, \beta, f_{\text{fake}}$) with blue and orange contours for $z = 1.19$ and $z = 1.47$, respectively⁵. The parameter set with the minimum value of χ^2 for $z = 1.19$ is $(A_w, \beta, f_{\text{fake}}) = (1.10, 0.534, 0.140)$ while that for $z = 1.47$ is $(A_w, \beta, f_{\text{fake}}) = (1.17, 0.538, 0.139)$. With these sets of the best-fitting parameters, we derive the integral constraints as $w_\Omega = 0.110$ and $w_\Omega = 0.114$, for lower and higher redshifts, respectively. The best-fitting power-law model prediction for the measured correlation function, $(1 - f_{\text{fake}})^2(A_w \theta^{-\beta} - w_\Omega)$, is

⁵ To show parameter constraints using the MCMC sampling here and in the rest of this paper, we use a python package `pygtc` (Bocquet & Carter 2016).

shown by the blue line in figure 2. The constrained parameters are shown in table 2.

When the two parameters for a power-law model of the angular correlation, (A_w, β), are known, one can determine its 3-dimensional clustering, $\xi(r) = (r/r_0)^{-\gamma}$, as (Peebles 1980; Efsthathiou et al. 1991; Simon 2007)

$$A_w = r_0^\gamma \left(\frac{10800}{\pi} \right)^{\gamma-1} B\left(\frac{1}{2}, \frac{\gamma-1}{2}\right) \int_0^\infty dx p^2(x) x^{1-\gamma}$$

$$= r_0^\gamma \frac{10800^{\gamma-1} (x_{\text{max}}^{\gamma-1} - x_{\text{min}}^{\gamma-1})}{\pi^{\gamma-1} (2-\gamma)(x_{\text{max}} - x_{\text{min}})^2} B\left(\frac{1}{2}, \frac{\gamma-1}{2}\right), \quad (15)$$

$$\beta = \gamma - 1, \quad (16)$$

where B is the beta function. The final expression of A_w is derived using the constant radial selection function [equation (10)]. As a result, the clustering length is constrained to be $r_0 = 4.12^{+0.50}_{-0.41}$ at $z = 1.19$ and $r_0 = 4.61^{+0.51}_{-0.45}$ at $z = 1.47$. These values correspond to the host halo masses of $M \gtrsim 10^{12} M_\odot/h$ and are roughly consistent with the preceding results of ELG clustering (see e.g., Kashino et al. 2017). Here we do not make a detailed comparison with previous works nor argue the clustering evolution further because the power-law model is not so accurate to be used to interpret the precise correlation function measurement anyways. In section 5, we discuss physical properties of halos hosting ELGs based on an HOD model that is much more sophisticated than the power-law model.

4.3 Linearly biased dark matter model

Next, we consider another simple model, the non-linear correlation function with the linear galaxy bias factor (Kaiser 1984),

$$\xi(r; b) = b^2 \xi_m(r), \quad (17)$$

where ξ_m is the underlying matter correlation function. We use the fitting formula of Takahashi et al. (2012) to compute the nonlinear matter power spectrum, $P_m(k)$, and then Fourier transform it to obtain ξ_m . Given equation (17), a similar form is derived for the angular correlation function as

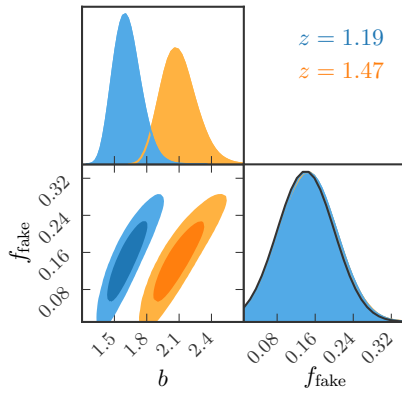


Fig. 4. Constraints on the linear galaxy bias b of the nonlinear dark matter model and the fake line fraction parameter f_{fake} for $z = 1.19$ (blue) and $z = 1.47$ (orange). Contours show the 68% and 95% confidence levels. The diagonal panel show the posterior probability distribution of each parameter. A Gaussian prior is adopted for the fake line fraction, $f_{\text{fake}} = 0.140 \pm 0.060$, which is shown as the black curve compared with the one-dimensional posterior. The posterior of f_{fake} for $z = 1.47$ (orange) is almost entirely behind the one for $z = 1.19$.

$$w(\theta; b) = b^2 w_m(\theta), \quad (18)$$

where w_m is the angular correlation function of matter, calculated using equation (9) with $\xi(r)$ replaced by the 3-dimensional matter correlation function, $\xi_m(r)$. In this model there are two free parameters to be determined, $\Theta = (b, f_{\text{fake}})$. This model is valid for a wider range of angular scales than the single power-law model. The data at the scales $0.0025 < \theta < 1$ [deg] are used to calculate the χ^2 statistic ($N_{\text{bin}} = 13$).

The joint constraints on (b, f_{fake}) are shown in figure 4. We find the best-fitting value of the bias parameter, $b = 1.61^{+0.13}_{-0.11}$ and $b = 2.09^{+0.17}_{-0.15}$, respectively for the lower and higher redshift measurements. These bias values can be compared to the effective bias b_{eff} to be determined by a HOD modeling [equation (27)]. The integral constraint is calculated by these best-fitting parameter sets for the correlation in the combined field as $w_\Omega = 0.0270$ and $w_\Omega = 0.0277$ for $z = 1.19$ and 1.47, respectively.

The best-fitting linearly-biased dark matter model, $(1 - f_{\text{fake}})^2 (b^2 w_m(\theta) - w_\Omega)$, is shown as the red solid curve in figure 2. To see the contribution of the integral constraint, we show the same model without w_Ω term, $(1 - f_{\text{fake}})^2 b^2 w_m(\theta)$, as the red dashed curve. As expected, the model correlation function is positive over all the scales studied here. As a reference, the dark matter correlation function, w_m , is shown by the black dashed curve in figure 2.

The relatively large uncertainties on the bias parameter comes from our conservative prior on f_{fake} . To see this, let us directly constrain the observed amplitude by considering the relation:

$$\hat{w}(\theta; \tilde{b}) = \tilde{w}(\theta; \tilde{b}) - \tilde{w}_\Omega(\tilde{b})$$

$$= \tilde{w}(\theta; \tilde{b}) - \frac{\sum_i \tilde{w}(\theta_i; \tilde{b}) RR(\theta_i)}{\sum_i RR(\theta_i)}, \quad (19)$$

where \tilde{b} is the bias parameter of the observed field, $\tilde{w}(\theta; \tilde{b}) = \tilde{b}^2 w_m(\theta)$. Equation (19) becomes equivalent to equations (6) and (18) if we set $\tilde{b} \equiv (1 - f_{\text{fake}})b$. By adopting this 1-parameter linearly-biased dark matter model, we obtain tighter constraints as $\tilde{b} = 1.379^{+0.042}_{-0.043}$ and $\tilde{b} = 1.786^{+0.052}_{-0.054}$ at $z = 1.19$ and $z = 1.47$, respectively, without any prior.

In the next subsection we further analyze the [OII] emitter samples with different luminosity and stellar mass thresholds using the linearly-biased DM model.

4.4 Line luminosity and stellar mass dependences of [OII]-emitter clustering

It is interesting to see how the amplitude of a measured correlation function depends on properties of the [OII] emitters. Here we consider two basic properties, the luminosity of the [OII] emission line and the stellar mass of the host galaxies, and split our sample into subsamples based on these thresholds.

Figure 5 shows the angular correlation functions measured with different line luminosity cuts. For clarity, we add the integral constraint correction so that all the correlation functions become positive at all scales probed. For each correlation function, we perform a model fitting using the linearly biased dark matter model considered in section 4.3. The best-fitting model for each measurement, $(1 - f_{\text{fake}})^2 b^2 w_m(\theta)$, is presented by the dashed curve. As discussed in section 4.3, this simple model fails to explain the measured correlation function at small scales. To see the dependence of the clustering amplitude on the luminosity, we constrain the parameter \tilde{b} in equation (19) as a function of the minimum line luminosity L_{min} . The result is shown in the left panel of figure 6. For each redshift, we find that the bias b increases with increasing line luminosity, by $\sim 10\%$. If the fake line fraction, f_{fake} , changed significantly with the luminosity, this luminosity dependence would be modulated.

We repeat the same analysis by splitting our [OII] emitter sample into subsamples with stellar mass cuts $M_{*,\text{min}}$. We measure the angular correlation function of [OII] emitters with the stellar mass of $M_* \geq M_{*,\text{min}}$. Since the fitting result for $w(\theta)$ is similar to that with the luminosity cuts in figure 5, we do not plot the figure. We constrain the measured clustering amplitude \tilde{b} as a function of $M_{*,\text{min}}$, as shown in the right panel of figure 6. A trend similar to the line luminosity limited samples is found: [OII] emitters with higher stellar masses cluster more strongly than those with lower masses. Almost no mass dependence is seen in the clustering at $z = 1.47$. As discussed in section 3.6 of Hayashi et al. (2018), multi-band data at longer wavelength, such as near-infrared data, would be required to accurately esti-

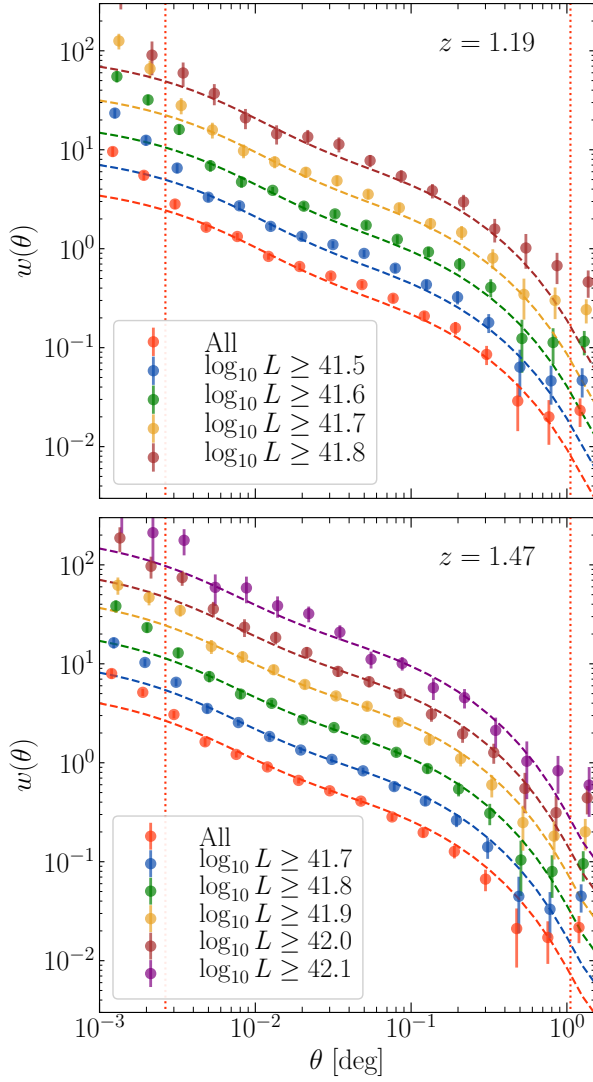


Fig. 5. Angular correlation functions of [OII] emitters at $z = 1.19$ (top) and $z = 1.47$ (bottom) with different peak luminosity cuts. The unit of L in the legend is $[\text{erg s}^{-1}]$. For the visualization purpose, the integral constraint is taken into account, and thus the vertical axis presents $\hat{w} + (1 - f_{\text{fake}})^2 w_{\Omega}$. The amplitudes of the correlation functions shown by the blue, green, yellow, brown and purple points are multiplied by 2^n where $n = 1, 2, \dots, 5$, respectively. The dashed curves are the best-fitting models of the linearly-biased dark matter model, $(1 - f_{\text{fake}})^2 b^2 w_m(\theta)$.

mate the stellar masses at $z \sim 1.5$. Thus, our result for the stellar mass dependence of the clustering at $z = 1.47$ needs to be interpreted with caution. Overall, however, the dependence of clustering of [OII] emitters on stellar masses is not as strong as that on line luminosities, which is qualitatively consistent with the result of Khostovan et al. (2018).

5 Dark matter-[OII] emitter connections

The halo occupation distribution (HOD) modeling is an empirical and parametric way to describe the connection between

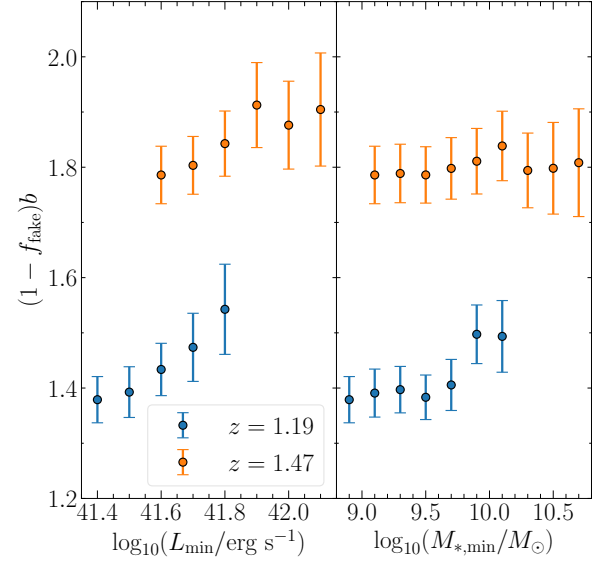


Fig. 6. Constraints on the measured clustering amplitude of [OII] emitters, $\hat{b} = (1 - f_{\text{fake}})b$, as a function of the minimum peak luminosity L_{min} (left) and stellar mass $M_{*,\text{min}}$ (right). The blue and orange points are the results at $z = 1.19$ and $z = 1.47$, respectively.

galaxies and their host halos through the modeling of the abundance and clustering of galaxies (Jing et al. 1998; Peacock & Smith 2000; Seljak 2000; Ma & Fry 2000; Scoccimarro et al. 2001; Cooray & Sheth 2002; Berlind & Weinberg 2002; Zheng et al. 2005; van den Bosch et al. 2013; Hikage et al. 2013; Okumura et al. 2015). In this section we use HOD modeling to investigate physical properties of halos which host [OII] emitters.

5.1 Formalism of halo model

The mean number of galaxies residing in a halo of mass M , denoted as $\langle N(M) \rangle$, is decomposed into central and satellite components,

$$\langle N(M) \rangle = \langle N_{\text{cen}}(M) \rangle + \langle N_{\text{sat}}(M) \rangle. \quad (20)$$

Once the HOD model is specified, the average number density of galaxies is calculated as

$$n_g = \int \langle N(M) \rangle n(M) dM, \quad (21)$$

where $n(M)dM$ is the halo mass function.

In a halo model approach, the power spectrum of galaxies, $P(k)$ where k is the wavenumber, can be decomposed into the one- and two-halo terms,

$$P(k) = P_{1h}(k) + P_{2h}(k). \quad (22)$$

The one-halo term can be further decomposed into contributions from the clustering of central-satellite and satellite-satellite pairs hosted by the same halos, namely,

$$P_{1h}(k) = \frac{1}{n_g^2} \int n(M) dM [2 \langle N_{\text{cen}} N_{\text{sat}} \rangle u(k, M) + \langle N_{\text{sat}} (N_{\text{sat}} - 1) \rangle u^2(k, M)], \quad (23)$$

where $u(k, M)$ describes the Fourier transform of the density profile of satellite galaxies within dark matter halos, which is assumed to follow the matter density profile. We assume that N_{sat} follows the Poisson statistics such that $\langle N_{\text{sat}} (N_{\text{sat}} - 1) \rangle = \langle N_{\text{sat}} \rangle^2$. We also assume that the occupation numbers of central and satellite galaxies are independent, i.e., $\langle N_{\text{cen}} N_{\text{sat}} \rangle = \langle N_{\text{cen}} \rangle \langle N_{\text{sat}} \rangle$. The two-halo term can be similarly decomposed into central-central, central-satellite and satellite-satellite galaxy pairs hosted by distinct halos,

$$P_{2h}(k) = \frac{1}{n_g^2} \int n(M) dM \int n(M') dM' \times [\langle N_{\text{cen}} \rangle + \langle N_{\text{sat}} \rangle u(k, M)] \times [\langle N_{\text{cen}} \rangle + \langle N_{\text{sat}} \rangle u(k, M')] P_{hh}(k; M, M'), \quad (24)$$

where $P_{hh}(k; M, M')$ is the cross-power spectrum of halos with masses M and M' . The halo mass function is calculated using the model derived by Tinker et al. (2010). The density profile of halos is assumed to have the NFW profile (Navarro et al. 1997) with the concentration given by Duffy et al. (2008). We compute P_{hh} as a product of the nonlinear matter power spectrum (Takahashi et al. 2012) and the halo bias,

$$P_{hh}(k; M, M') = b_h(M) b_h(M') P_m(k), \quad (25)$$

where $b_h(M)$ is the bias for a halo of mass M . We use the large-scale halo bias $b_h(M)$ proposed also by Tinker et al. (2010).

The three-dimensional correlation function of galaxies is calculated by a Fourier transform of the power spectrum,

$$\xi(r) = \frac{1}{2\pi^2} \int_0^\infty dk k^2 P(k) \frac{\sin kr}{kr}. \quad (26)$$

Then the angular correlation function is finally obtained through equation (9).

In addition to the number density, given a set of HOD parameters, one can determine various physical quantities such as the effective bias,

$$b_{\text{eff}} = \frac{1}{n_g} \int b_h(M) \langle N(M) \rangle n(M) dM, \quad (27)$$

the effective halo mass,

$$M_{\text{eff}} = \frac{1}{n_g} \int M \langle N(M) \rangle n(M) dM, \quad (28)$$

and the satellite fraction,

$$f_{\text{sat}} = \frac{1}{n_g} \int \langle N_{\text{sat}}(M) \rangle n(M) dM. \quad (29)$$

5.2 Halo occupation distribution model for [OII] emitters

In this paper we adopt the HOD model developed by Geach et al. (2012) to describe the population of ELGs (see also Kim et al. 2011; Contreras et al. 2013). In this model, the central HOD is described by two components:

$$\langle N_{\text{cen}}(M) \rangle = F_c^B (1 - F_c^A) \exp \left[-\frac{\log(M/M_c)^2}{2(\sigma_{\log M})^2} \right] + F_c^A \left[1 + \text{erf} \left(\frac{\log(M/M_c)}{\sigma_{\log M}} \right) \right], \quad (30)$$

where $F_c^{A,B}$ are normalization factors. The first component describes the Gaussian distribution of centrals around halos of average mass M_c with the dispersion $\sigma_{\log M}$, and the second component describes the standard mass-limited step function form proposed by Zheng et al. (2005) (see section 5.5 below). The satellite HOD is given by

$$\langle N_{\text{sat}}(M) \rangle = F_s \left[1 + \text{erf} \left(\frac{\log(M/M_{\text{min}})}{\delta_{\log M}} \right) \right] \left(\frac{M}{M_{\text{min}}} \right)^\alpha, \quad (31)$$

where F_s is the mean number of satellites per halo at the transition mass M_{min} which corresponds to the characteristic mass above which halos can contain satellites, $\delta_{\log M}$ is the width of the transition from zero satellites per halo to the power law, and α is the slope of the power law which gives the mean number of satellites for $M > M_{\text{min}}$. We refer the reader to Geach et al. (2012) and Contreras et al. (2013) for a more detailed explanation of this model.

We fix the least-important parameter, $\delta_{\log M}$, to $\delta_{\log M} = 1$. Thus the number of free parameters in the Geach HOD model together with the fake line fraction is eight, $\Theta = (M_c, M_{\text{min}}, \sigma_{\log M}, \alpha, F_c^A, F_c^B, F_s, f_{\text{fake}})$. The parameter α is known to have a value around unity. We thus apply a Gaussian prior on α as $\alpha = 1.00 \pm 0.20$. As with the analysis in section 4, we further impose a Gaussian prior on the fake line fraction parameter as $f_{\text{fake}} = 0.140 \pm 0.060$. Uniform priors are applied for the other 6 parameters. Table 3 summarizes the priors on all the eight parameters. We use the Python package HALOMOD (Murray et al. 2013) to calculate the HOD model prediction for the angular correlation function.

5.3 HOD parameter constraints

We present constraints on the HOD model using the measured angular correlation function of the [OII] emitters. We compute the χ^2 statistic for the HOD model constructed from the observed angular correlation function, χ_w^2 , and number density, χ_n^2 , as

$$\chi^2(\Theta) = \chi_w^2(\Theta) + \chi_n^2(\Theta), \quad (32)$$

where χ_w^2 is given by equation (13) and χ_n^2 is given by

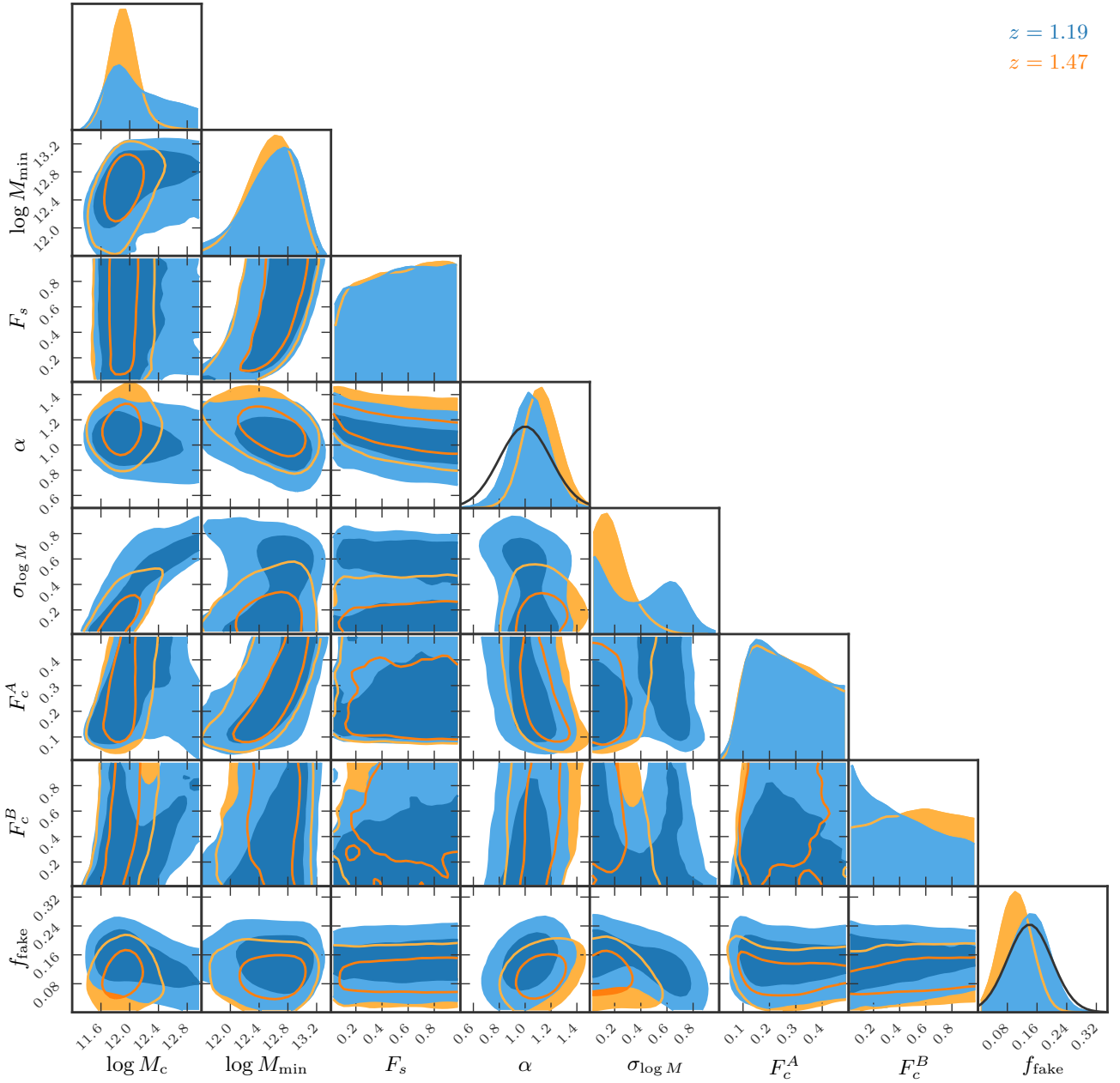


Fig. 7. Constraints on parameters of Geach HOD model, $(\log M_c, \log M_{\min}, \alpha, \sigma_{\log M}, F_s, F_c^A, F_c^B)$ and f_{fake} for $z = 1.19$ (blue) and $z = 1.47$ (orange). Two-dimensional contours show the 68% and 95% confidence levels after the other six parameters marginalized over. The diagonal panels show the posterior probability distribution of each parameter. Gaussian priors are assumed for α and f_{fake} , as depicted by the black solid curves in the 1-d posterior panels.

$$\chi_n^2(\Theta) = \frac{[\log n_g^{\text{obs}} - \log n_g^{\text{th}}(\Theta) + \log(1 - f_{\text{fake}})]^2}{\sigma_{\log n_g}^2}, \quad (33)$$

where $\Theta = (\log M_c, \log M_{\min}, \alpha, \sigma_{\log M}, F_s, F_c^A, F_c^B, f_{\text{fake}})$. Since the observed number of [OII] emitters includes non-[OII] contaminants characterized by the fraction f_{fake} , we need to take into account a factor of $(1 - f_{\text{fake}})$ difference between the observed number density and its theoretical prediction computed by equation (21). As shown in table 1, the observed number density is $n_g^{\text{obs}} = 5.50 \times 10^{-3} (h/\text{Mpc})^3$ at $z = 1.19$

and $n_g^{\text{obs}} = 4.08 \times 10^{-3} (h/\text{Mpc})^3$ at $z = 1.47$. We set the uncertainty of $\log n_g^{\text{obs}}$ as $\sigma_{\log n_g} = 0.03 |\log n_g^{\text{obs}}|$ following the measurement uncertainty of the luminosity function (Hayashi et al. 2020). Due to the flexibility of the model, the HOD enables us to fit an observed correlation function over a broader range than the power-law and nonlinear dark matter models considered in the previous section. We thus use the data at $0.0015 < \theta < 1$ [deg] and the number of angular separation bins is $N_{\text{bin}} = 14$. Together with the number density, the degree of freedom is $\nu = N_{\text{bin}} + 1 - 8 = 7$.

Table 3. Priors and constraints of the HOD parameters for Geach model*

Parameter	Prior	NB816		NB921	
		Best-fit	Posterior PDF	Best-fit	Posterior PDF
$\log M_c/(h^{-1}M_\odot)$	None	11.75	$12.04^{+0.57}_{-0.32}$	11.93	$11.91^{+0.19}_{-0.18}$
$\log M_{\min}/(h^{-1}M_\odot)$	None	12.46	$12.61^{+0.32}_{-0.43}$	12.47	$12.57^{+0.29}_{-0.35}$
$\sigma_{\log M}$	[0, 1]	0.06	$0.40^{+0.28}_{-0.31}$	0.13	$0.17^{+0.15}_{-0.10}$
α	1.00 ± 0.20	1.06	$1.03^{+0.12}_{-0.13}$	1.23	$1.12^{+0.13}_{-0.12}$
F_c^A	[0, 0.5]	0.13	$0.26^{+0.16}_{-0.12}$	0.14	$0.26^{+0.15}_{-0.13}$
F_c^B	[0, 1]	0.95	$0.37^{+0.39}_{-0.28}$	0.90	$0.53^{+0.32}_{-0.34}$
F_s	[0, 1]	0.98	$0.54^{+0.31}_{-0.34}$	0.73	$0.55^{+0.31}_{-0.33}$
f_{fake}	0.140 ± 0.060	0.172	$0.140^{+0.048}_{-0.053}$	0.128	$0.104^{+0.043}_{-0.041}$
χ^2/ν ($\nu = 7$)		2.17		0.856	
Inferred quantity	Measurement	Best-fit	Posterior PDF	Best-fit	Posterior PDF
$\log n_g/(h^{-1}\text{Mpc})^{-3}$	-2.259 ± 0.068 (NB816) -2.344 ± 0.070 (NB921)	-2.313	$-2.316^{+0.071}_{-0.073}$	-2.401	$-2.381^{+0.074}_{-0.073}$
f_{sat}	...	0.308	$0.159^{+0.120}_{-0.047}$	0.242	$0.159^{+0.109}_{-0.049}$
b_{eff}	...	1.797	$1.700^{+0.084}_{-0.111}$	2.029	$1.981^{+0.072}_{-0.068}$
$\log M_{\text{eff}}/(h^{-1}M_\odot)$...	12.831	$12.703^{+0.093}_{-0.071}$	12.699	$12.609^{+0.085}_{-0.051}$

* In the ‘‘Prior’’ column the ranges specified in brackets are for uniform priors while the others we quote the mean and standard deviation of the Gaussian priors. The column of ‘‘Best-fit’’ shows the parameter set which gives the minimum value of χ^2 . In the column of ‘‘Posterior PDF’’, the central value is a median and the error means 16 – 84 percentiles after other parameters are marginalized over. The measured number density $\log n_g$ includes non-[OII] emitters, and thus its best-fitting values differ from the measure ones by $\log(1 - f_{\text{fake}}) \sim -0.06$.

The resulting constraints on the HOD parameters of the Geach model are shown in figure 7. This and the following two figures are the main results of this paper. The eight dimensional posterior distributions are visualized in two-dimensional contours with the other six parameters marginalized over. The top row of each column shows the one-dimensional posterior. The constraints are summarized in table 3. The normalizations parameters, F_c^A, B and F_s , are poorly constrained, which are expected and consistent with Geach et al. (2012) and Hong et al. (2019). Overall, constraints from the $z = 1.47$ sample are tighter than those from the $z = 1.19$ one. Particularly, the marginalized distribution for $\sigma_{\log M}$ for the $z = 1.19$ sample is much wider and even becomes bimodal. Interestingly, this bimodality was seen by Hong et al. (2019) who analyzed the clustering of Ly α emitters using the Geach HOD model. Although there are many free parameters with few priors, we obtain meaningful constraints due to our large sample. Particularly strong constraints are obtained for the two mass parameters, M_c and M_{\min} as seen in table 3, because M_c can be determined by the observed number density, n_g , and M_{\min} primarily degenerates with M_c . We do not see a strong evolution of HOD from $z = 1.47$ to 1.19, which is consistent with our ongoing work based on cosmological hydrodynamical simulations (Osato & Okumura 2021).

The posterior distribution of the HOD is shown in figure 8. The dark and light shaded regions show the 68 and 95% confidence intervals for the total HOD, respectively, and red solid curve is the median. The black solid curve is the HOD with a

set of parameters which give the minimum χ^2 value in the eight dimensional parameter space. The HOD with the minimum χ^2 looks somewhat different from the median of the HOD, particularly the central HOD. This is a similar trend with the finding of Hong et al. (2019). They found that two independent algorithms give very different best-fitting HOD parameters (See Model#1 and Model#2 of their figure 7). This small but non-negligible discrepancy largely comes from the fact that the normalization parameters, especially F_c^B , and the scatter of the mass, $\sigma_{\log M}$, are poorly constrained. Even though the HODs are different, the predicted angular correlation functions with these HOD parameter sets become very similar.

The best-fitting Geach HOD model prediction, $(1 - f_{\text{fake}})^2(w(\theta; \Theta) - w_\Omega)$, is shown as the red solid curve in figure 9. The contributions from the 1-halo and 2-halo components are shown as the blue and green curves, respectively. Obviously, agreement of the measured correlation function with the HOD model prediction is much more remarkable than that with the power-law or linearly biased dark matter model, compared to figure 2.

5.4 Derived physical parameters for host halos

Using the constrained HOD parameters, one can infer the parameters which characterize the properties of [OII] emitters and their host dark matter halos, such as the galaxy number density, effective halo bias and mass, and satellite galaxy fraction,

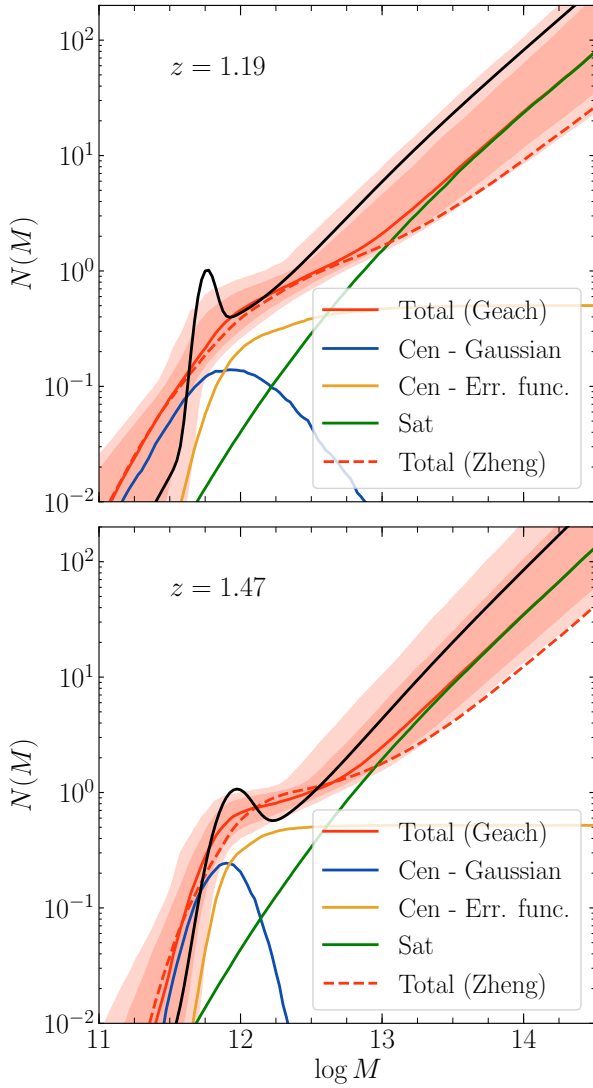


Fig. 8. HOD with the best-fitting parameters of Geach model at $z = 1.19$ (top) and $z = 1.47$ (bottom). The blue and yellow lines show the average numbers of centrals from the Gaussian and error function terms (see equation (30)), while the green line shows that of satellites. The red solid line is the sum of the blue, yellow and green lines, the average number of all the [OII] emitters. The dark and light red shaded regions indicate the 68% and 95% confidence intervals. The red dashed curve is the same as the red solid curve but for the best-fitting HOD of Zheng et al. (2005). For comparison, the black curve shows the HOD of the Geach model which gives the minimum χ^2 value.

through equations (21), (27), (28), and (29), respectively. The posterior distribution for these parameters is shown in figure 10 and summarized in table 3. The number density is constrained following the imposed prior. Note again that the constrained number density is different from the observed number density by a factor of $(1 - f_{\text{fake}})$, $n_g^{\text{th}} = (1 - f_{\text{fake}})n_g^{\text{obs}}$. The effective bias parameter is determined at $z = 1.19$ and 1.47 as $b_{\text{eff}} = 1.701^{+0.083}_{-0.110}$ and $b_{\text{eff}} = 1.981^{+0.072}_{-0.068}$, respectively. They are fully consistent with the linear bias parameter from much simpler analysis in section 4.3, $b = 1.61^{+0.13}_{-0.11}$ and $b = 2.09^{+0.17}_{-0.15}$.

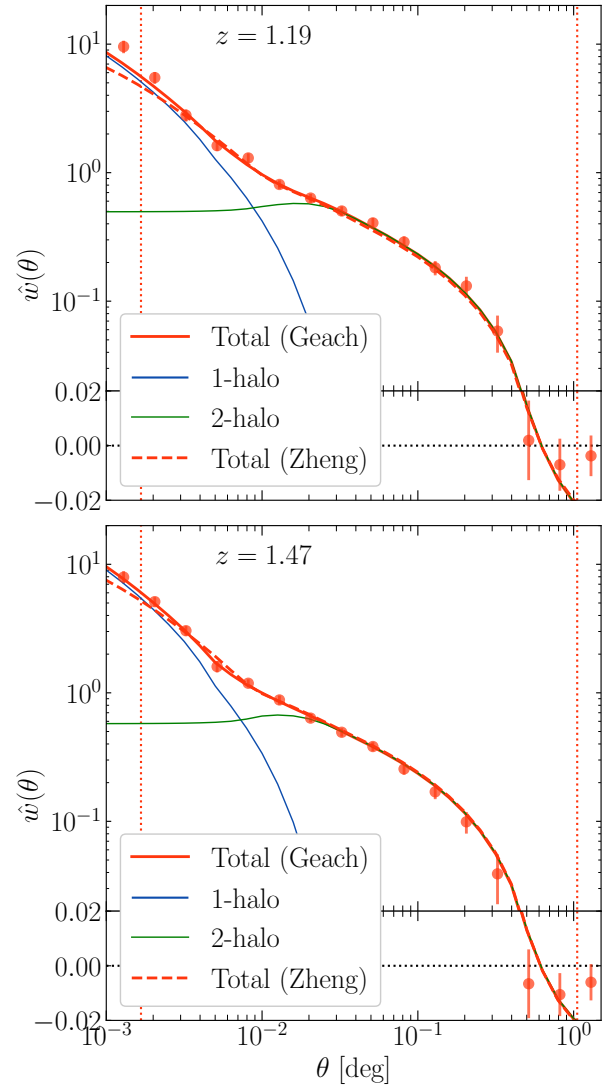


Fig. 9. The angular correlation functions of [OII] emitters at $z = 1.19$ (top) and $z = 1.47$ (bottom). Note that the vertical axis mixes logarithmic and linear scalings. The red points are the measurement, \hat{w} , the same as those in figure 2. The blue and green solid curves are the one- and two-halo terms with the best-fitting Geach HOD model, respectively, and the red solid curve is their sum. For comparison, we also show the best-fitting Zheng HOD model as the red dashed curve. The data enclosed by the two red vertical lines are used for this HOD analysis.

The effective masses of halos hosting [OII] emitters are derived to be $\log M_{\text{eff}}/(h^{-1}M_{\odot}) = 12.703^{+0.091}_{-0.069}$ and $12.609^{+0.085}_{-0.051}$ at $z = 1.19$ and 1.47 , respectively. Figure 11 shows the constraints on M_{eff} as a function of redshift obtained from our HSC [OII] emitters together with the previous studies at $0 < z < 4$ which were already presented in Kashino et al. (2017). The constraints include the studies of photo- z galaxies from the CFHT Legacy Survey at $z \sim 0.3, 0.5$ and 0.7 (Coupon et al. 2012), VIMOS-VLT Deep Survey (VVDS) at $z \sim 0.55$ and 1 (Abbas et al. 2010), NEWFIRM Medium Band Survey at $z \sim 1.1$ and 1.5 (Wake et al. 2011), $H\alpha$ emitters from the

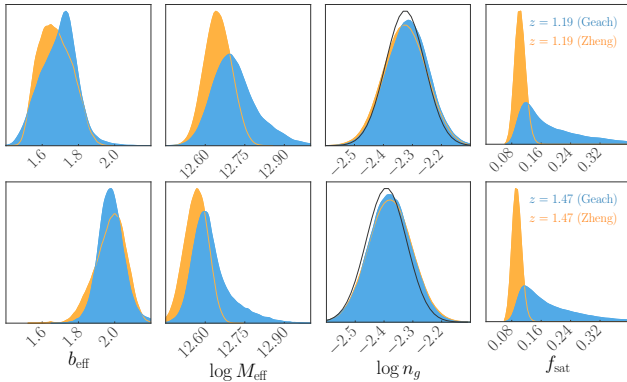


Fig. 10. Posterior distribution for the parameters derived from the best-fitting parameters for the Geach (blue) and Zheng (orange) HOD models. From the left to right, the posteriors for the effective bias, effective halo mass, the galaxy number density and the satellite fraction are shown. The upper and lower panels show results for $z = 1.19$ and $z = 1.47$, respectively. The number density presented here is different from the observed number density shown in table 1 by a factor of $(1 - f_{\text{fake}})$, $(1 - f_{\text{fake}})n_g^{\text{obs}}$ (see table 3 for the constrained values for f_{fake}). Gaussian priors assumed for $\log n_g$ are depicted by the black solid curves, where the best-fitting value of f_{fake} is adopted to multiply by $(1 - f_{\text{fake}})$. The posterior of $\log n_g$ for $z = 1.47$ (orange) is almost entirely behind the one for $z = 1.19$.

FMOS-COSMOS Survey at $z \sim 1.6$ (Kashino et al. 2017) and from the HiZELS survey at $z \sim 2.2$ (Geach et al. 2012), and VUDS at $z \sim 2.5$ and 3.5 (Durkalec et al. 2015). These samples have number densities and stellar masses similar to our [OII] emitter samples. Here we also plot the average mass assembly history of halos with different present-day masses, as derived by Behroozi et al. (2013) based on an N -body simulation. According to this prediction, our measurements of M_{eff} at two redshifts are well explained by the mass-assembly history with $M(z=0) = 1.5 \times 10^{13} M_{\odot}/h$ as depicted by the blue solid curve. The effective halo mass of [OII] emitters at $z = 1.47$ is slightly higher than the blue curve, which reflects the fact that [OII] emitters of our $z = 1.47$ sample are intrinsically brighter than those of the lower- z sample (see section 2.2). Given the accurate constraints on HOD, one can in principle infer the mass of the host halo for an individual emission line galaxy (Oguri & Lin 2015). It is, however, beyond the scope of this paper and will be investigated in future work.

For our [OII] emitter sample, the satellite galaxy fraction is constrained as $f_{\text{sat}} = 0.158^{+0.114}_{-0.047}$ and $0.159^{+0.109}_{-0.049}$ at $z = 1.19$ and 1.47 , respectively. The preceding studies revealed that the satellite galaxy fraction of a given population would depend on the redshift, number density and stellar mass (Coupon et al. 2012; Guo et al. 2014; Guo et al. 2019). At least over the redshift we studied here, the satellite fraction of [OII] emitters in our sample does not significantly evolve with redshift. The analysis of Favole et al. (2016) constrained the satellite fraction of ELGs with the host halo mass $M \sim 10^{12} h^{-1} M_{\odot}$ as $f_{\text{sat}} = 0.225 \pm 0.025$. Avila et al. (2020) constrained the value

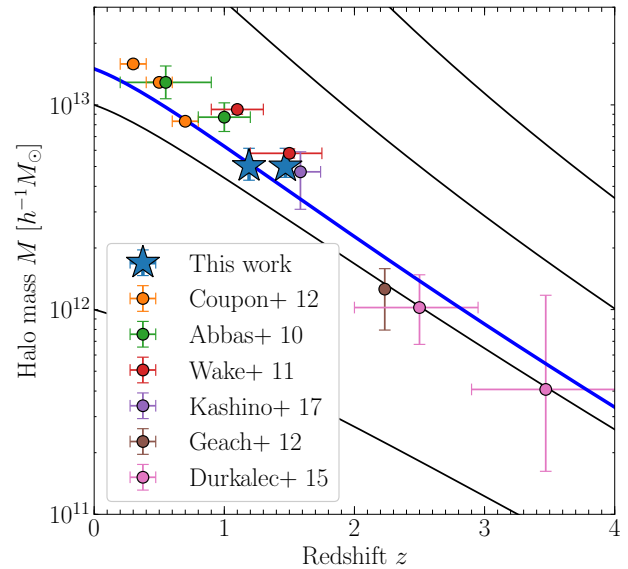


Fig. 11. Average mass of halos hosting ELGs as a function of redshift. The blue stars are the result from our analysis of [OII] emitters at $z = 1.19$ and $z = 1.47$. The other points are the results of the previous HOD analysis by Abbas et al. (2010), Wake et al. (2011), Geach et al. (2012), Coupon et al. (2012), Durkalec et al. (2015), and Kashino et al. (2017) (see the legend). The solid curves show a prediction of mass accretion histories for halos with $M(z=0) = 10^{15}, 10^{14}, 10^{13}$ and $10^{12} M_{\odot}$ from the top to bottom (Behroozi et al. 2013). The blue curve represents the one with $M(z=0) = 1.5 \times 10^{13} [h^{-1} M_{\odot}]$.

of f_{sat} for ELGs from the eBOSS survey, and the best fitting value of their baseline model is $f_{\text{sat}} = 0.22$, consistent with our measurements. However, their constraints are significantly model-dependent and varying the baseline model changes the best-fitting value between $0.18 \leq f_{\text{sat}} \leq 0.70$. Moreover, the selection of ELGs in the eBOSS survey is quite different from ours based on the NB. We thus cannot make a quantitative comparison with their result. Guo et al. (2019) further studied the relation among the satellite fraction, stellar mass and halo mass for ELGs from the eBOSS survey. They showed that the host halo mass of ELGs with $f_{\text{sat}} \sim 0.15$ is $\log M/(h^{-1} M_{\odot}) \sim 12.6$ is a strong function of the stellar mass. It provides good agreement with our clustering measurements of [OII] emitters from the HSC survey.

5.5 Comparison to a simpler HOD

While the Geach HOD model is general and flexible, as a trade-off, the HOD parameters are constrained more poorly and more degenerated with each other. Furthermore, it is not clear whether different halo occupation functions provide the same physical interpretation for a measured correlation function. A similar attempt has been made by studying one of the simplest HOD model (Zehavi et al. 2005) in Hong et al. (2019) (see their Appendix B). Here we investigate whether the predicted cor-

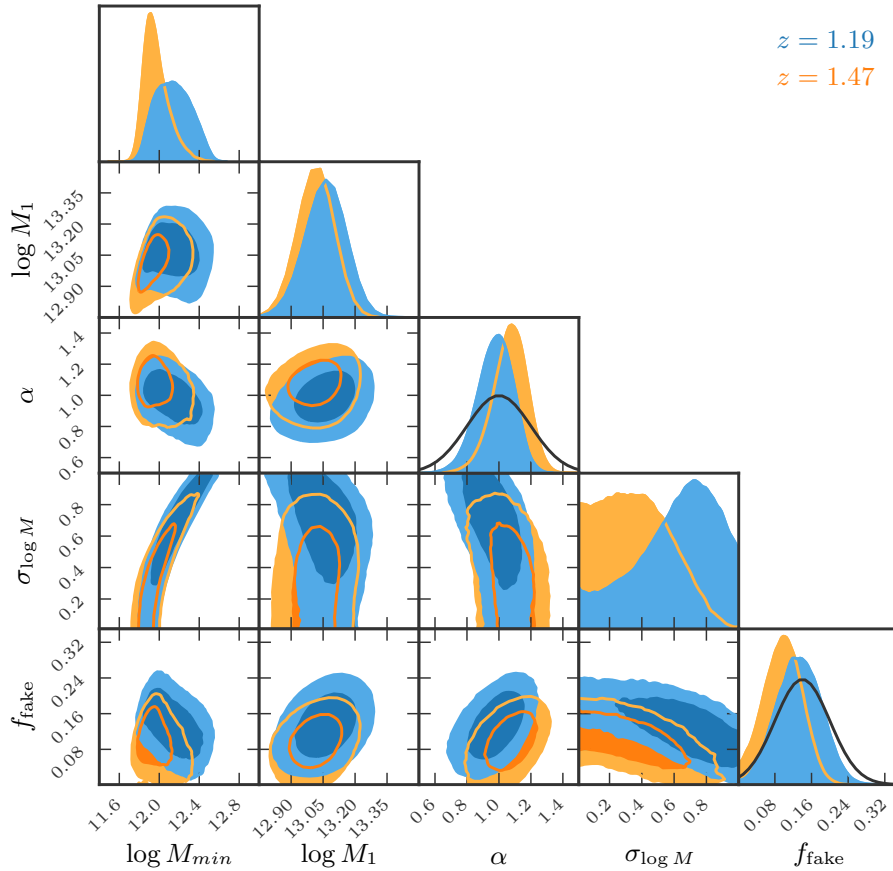


Fig. 12. Constraints on HOD parameters of Zheng’s model, $(\log M_c, \log M_{\min}, \alpha, \sigma_{\log M})$ and f_{fake} for $z = 1.19$ (blue) and $z = 1.47$ (orange). Contours show the 68% and 95% confidence levels. The diagonal panels show the posterior probability distribution of each parameter. Gaussian priors are assumed for α and f_{fake} , as depicted by the black curves in the panels of the 1-d posterior distributions.

relation function, halo occupation function, and the host halo parameters of [OII] emitters can be different between different HOD models.

To see this, we consider the commonly-adopted model of Zheng et al. (2005) (see also Zheng et al. 2007). The model contains five parameters in total and the central and satellite HODs are, respectively, given by

$$N_{\text{cen}}(M) = \frac{1}{2} \left[1 + \text{erf} \left(\frac{\log M / M_{\min}}{\sigma_{\log M}} \right) \right], \quad (34)$$

$$N_{\text{sat}}(M) = \frac{1}{2} \left[1 + \text{erf} \left(\frac{\log M / M_{\min}}{\sigma_{\log M}} \right) \right] \left(\frac{M - M_0}{M_1} \right)^\alpha, \quad (35)$$

where M_{\min} is the characteristic mass to host a central galaxy, M_1 is a mass for a halo with a central galaxy to host one satellite, M_0 is the mass scale to truncate satellites, $\sigma_{\log M}$ is the characteristic transition width, and α is the slope of the power law for the satellite HOD, the same as α in the Geach model. The parameter M_0 is a poorly-constrained parameter. In order to make this analysis simpler, we impose a relation between M_0 and M_1 following Conroy et al. (2006) (see also Kashino et al. 2017),

$$\log M_0 / (h^{-1} M_\odot) = 0.76 \log M_1 / (h^{-1} M_\odot) + 2.3. \quad (36)$$

Thus the number of free parameters in the Zheng HOD model together with the fake line fraction is five, $\Theta = (M_{\min}, M_1, \sigma_{\log M}, \alpha, f_{\text{fake}})$. As is the case of the analysis with the Geach HOD model, we apply the Gaussian priors on α and f_{fake} as $\alpha = 1.00 \pm 0.20$ and $f_{\text{fake}} = 0.140 \pm 0.060$, and flat priors on the other 3 parameters. We use the data with the same angular separation range as the analysis of the Geach HOD model (section 5.3), $0.0015 < \theta < 1$ [deg], the degree of freedom is $\nu = N_{\text{bin}} + 1 - 5 = 10$.

The resulting constraints on the HOD parameters of Zheng’s model are shown in figure 12 and summarized in table 4. Overall, the constraints on the Zheng HOD model are tighter than those on the Geach model due to the fewer number of parameters. The posterior distribution of the HOD $N(M)$ is shown as the red dashed curve in figure 8. Interestingly, the two models predict very similar HODs, particularly the central ones, for the observed angular correlation function of [OII] emitters. The discrepancy seen at $M > 10^{13} M_\odot / h$ is reasonable because such massive halos are rare as hosts of [OII] emitters and since

Table 4. Priors and constraints of the HOD parameters for Zheng model*

Parameter	Prior	NB816		NB921	
		Best-fit	Posterior PDF	Best-fit	Posterior PDF
$\log M_{\min}/(h^{-1}M_{\odot})$	None	12.16	$12.14^{+0.19}_{-0.18}$	11.88	$11.95^{+0.15}_{-0.10}$
$\log M_1/(h^{-1}M_{\odot})$	None	13.070	$13.062^{+0.084}_{-0.090}$	13.000	$13.017^{+0.075}_{-0.078}$
$\sigma_{\log M}$	[0, 1]	0.68	$0.65^{+0.21}_{-0.32}$	0.18	$0.34^{+0.25}_{-0.23}$
α	1.00 ± 0.20	0.99	$0.98^{+0.11}_{-0.12}$	1.11	$1.07^{+0.10}_{-0.11}$
f_{fake}	0.140 ± 0.060	0.123	$0.133^{+0.048}_{-0.048}$	0.115	$0.098^{+0.041}_{-0.043}$
χ^2/ν ($\nu = 10$)		1.86		1.42	
Inferred quantity	Measurement	Best-fit	Posterior PDF	Best-fit	Posterior PDF
$\log n_g/(h^{-1}\text{Mpc})^{-3}$	-2.259 ± 0.068 (NB816) -2.344 ± 0.070 (NB921)	-2.327	$-2.325^{+0.075}_{-0.073}$	-2.369	$-2.379^{+0.075}_{-0.074}$
f_{sat}	...	0.100	$0.102^{+0.013}_{-0.012}$	0.098	$0.094^{+0.012}_{-0.011}$
b_{eff}	...	1.659	$1.668^{+0.102}_{-0.089}$	2.034	$1.983^{+0.077}_{-0.095}$
$\log M_{\text{eff}}/(h^{-1}M_{\odot})$...	12.645	$12.647^{+0.052}_{-0.050}$	12.591	$12.567^{+0.043}_{-0.046}$

* In the ‘‘Prior’’ column the ranges specified in brackets are for uniform priors while the others we quote the mean and standard deviation of the Gaussian priors. The column of ‘‘Best-fit’’ shows the parameter set which gives the minimum value of χ^2 . In the column of ‘‘Posterior PDF’’, the central value is a median and the error means 16 – 84 percentiles after other parameters are marginalized over. The measured number density $\log n_g$ includes non-[OII] emitters, and thus its best-fitting values differ from the measure ones by $\log(1 - f_{\text{fake}}) \sim -0.06$.

the varied range of F_s in the Geach model is $0 \leq F_s \leq 1$, the larger number of $\langle N_{\text{sat}} \rangle$ is allowed in the model (see the factor of 1/2 in the Zheng model). Furthermore, since the Zheng model has $\langle N_{\text{cen}} \rangle = 1$ at the high mass end, it would make sense for the Zheng model to have the lower number of $\langle N_{\text{sat}} \rangle$ when the total number density is fixed. Nevertheless, the two $N(M)$ ’s are consistent with each other within $2 - \sigma$. The best-fitting correlation function is shown as the red dashed curve in the upper and lower panels of figure 9 for $z = 1.19$ and $z = 1.47$, respectively. As expected, the overall shape of the correlation function is very similar with that of the Geach model depicted by the red solid curve. However, one can see that the Geach model shows a better fit to the measured $w(\theta)$ at the smallest scales, which would imply that the ELGs in our sample prefer the HOD model which allows massive halos to have no central ELG.

The posterior distribution of the derived physical parameters is shown by the function colored orange in figure 10. Since the number density is primarily constrained by our prior, the two models predict the same values. We find that the effective bias b_{eff} and halo mass $\log M_{\text{eff}}$ determined from the Zheng HOD model are also consistent with those from the Geach model within the statistical uncertainties. On the other hand, the satellite fraction is derived to be $f_{\text{sat}} = 0.102^{+0.013}_{-0.012}$ and $0.093^{+0.012}_{-0.011}$ at $z = 1.19$ and 1.47 , respectively. These values are slightly lower than those determined based on the Geach HOD model, respectively $0.158^{+0.114}_{-0.047}$ and $0.159^{+0.109}_{-0.049}$, though the differences are not significant. This again reflects the fact that the Geach model adopts a more flexible parameterization and the larger amplitude of $\langle N_{\text{sat}} \rangle$ is allowed. Hence the 1-d posterior of f_{sat} obtained from the Geach model has a long tail toward

the high f_{sat} end.

Overall, the differences of halo parameters for [OII] emitters determined from the Geach and Zheng HOD models are not significant compared to the current statistical uncertainties. However, such small differences need to be carefully treated in the future clustering analysis ELGs from large galaxy surveys such as the Subaru PFS, DESI, and Euclid surveys.

6 Summary

In this paper we have studied the clustering of emission line galaxies at $z > 1$ and physical properties of dark matter halos which host them. For this purpose we used [OII] emitters detected at $z = 1.19$ and 1.47 using two narrow band filters, NB816 and NB921, respectively, in the Subaru HSC survey (Hayashi et al. 2020). We then measured the angular correlation functions of 8302 ($z = 1.19$) and 9578 ($z = 1.47$) of [OII] emitters. Using a simple model of the nonlinear correlation function with the linear galaxy bias factor, we measured the bias of [OII] emitters as $b = 1.61^{+0.13}_{-0.11}$ and $2.09^{+0.17}_{-0.15}$ at $z = 1.19$ and 1.47 , respectively. We also found that the bias monotonically increases with the line luminosity.

We, for the first time, performed an HOD analysis for the measured correlation functions of [OII] emitters based on a model developed to describe the population of galaxies selected by a star forming rate (Geach et al. 2012). We varied eight parameters simultaneously with only a few priors. Nevertheless, the two HOD parameters related to the host halo mass have been well constrained given the large sample from the HSC survey.

Based on the constrained HOD parameters, we have de-

rived parameters which describe properties of the host halos of [OII] emitters, such as the effective bias, effective halo mass and satellite fraction. The effective biases are determined as $b_{\text{eff}} = 1.701_{-0.110}^{+0.083}$ and $1.981_{-0.068}^{+0.072}$ at $z = 1.19$ and 1.47 , respectively. They are consistent with the linear bias values determined based on a simple nonlinear dark matter model. The effective halo masses and satellite fractions are derived as $\log M_{\text{eff}}/(h^{-1}M_{\odot}) \simeq 12.7$ (12.6) and $f_{\text{sat}} \simeq 0.16$ (0.16) at $z = 1.19$ (1.47). They are consistent with the result of Guo et al. (2019) who studied the relation among f_{sat} , M_{eff} and the stellar mass using the ELG sample from the eBOSS survey. Furthermore, the determined effective halo masses are in good agreement with previous studies of similar tracers with the mass-assembly history with $M(z=0) = 1.5 \times 10^{13} h^{-1} M_{\odot}$.

As stated in section 1, ELGs will be a main tracer in large galaxy surveys at high redshifts. Particularly, [OII] emitters will be targeted by many ongoing/future surveys such as the Subaru PFS survey (Takada et al. 2014). The result presented in this paper is useful to construct a mock catalog for cosmological analysis. The physical properties of halos hosting [OII] emitters revealed in this paper can also be applicable to the Subaru PFS, DESI, and other forthcoming surveys.

In this analysis, both the shape of the angular correlation function and number density are constrained by the HOD modeling. However, there is a claim that in 3-dimensional analysis the HOD would fail to explain the redshift-space clustering and number density simultaneously (Reid et al. 2014; Saito et al. 2016). To investigate this, we need a spectroscopic survey, and we can do it with the PFS, DESI or *Euclid* surveys.

The NB data of the HSC-SSP PDR2 provide emission lines of not only [OII] but also H α and [OIII], ranging from $z \sim 0.4$ to $z \sim 1.6$ (Hayashi et al. 2020). Redshift evolution of physical properties such as the halo mass for ELGs using these multiple emission lines will be studied in our future work.

Acknowledgments

TO thanks the members of the Subaru PFS Cosmology Working Group, particularly Masahiro Takada, Eiichiro Komatsu, and Ryu Makiya for useful correspondences during the regular telecon. TO is grateful to Shogo Ishikawa for discussion. We also thank the anonymous referee for the careful reading and suggestions. TO acknowledges support from the Ministry of Science and Technology of Taiwan under Grants No. MOST 109-2112-M-001-027- and the Career Development Award, Academia Sinica (AS-CDA-108-M02) for the period of 2019-2023. KO is supported by JSPS Overseas Research Fellowships. This work is based on data collected at Subaru Telescope, which is operated by the National Astronomical Observatory of Japan.

The Hyper Suprime-Cam (HSC) collaboration includes the astronomical communities of Japan and Taiwan, and Princeton

University. The HSC instrumentation and software were developed by the National Astronomical Observatory of Japan (NAOJ), the Kavli Institute for the Physics and Mathematics of the Universe (Kavli IPMU), the University of Tokyo, the High Energy Accelerator Research Organization (KEK), the Academia Sinica Institute for Astronomy and Astrophysics in Taiwan (ASIAA), and Princeton University. Funding was contributed by the FIRST program from the Japanese Cabinet Office, the Ministry of Education, Culture, Sports, Science and Technology (MEXT), the Japan Society for the Promotion of Science (JSPS), Japan Science and Technology Agency (JST), the Toray Science Foundation, NAOJ, Kavli IPMU, KEK, ASIAA, and Princeton University.

Appendix 1 Correlation functions in individual fields

In order to confirm the consistency of the angular correlation functions among different fields, we present the measurement from each of the individual four fields, \hat{w}_k , as the black points in Figure 13. The square roots of the diagonal components of the covariance matrix, $C_{k,ii}^{1/2}$, are shown as the error bars. The results for $z = 1.19$ and $z = 1.47$ are shown in the upper and lower panels, respectively. In order to compare the correlation functions between different fields, we need to take into account the correction of the integral constraint because the survey volume of each field is different. To estimate the integral constraint for k -th field, $w_{\Omega,k}$, the random-random count for the field, RR_k , is used as RR in equation (11), and

$$w_{\Omega,k}(\Theta) = \frac{\sum_i w(\theta_i; \Theta) RR_k(\theta_i)}{\sum_i RR_k(\theta_i)}. \quad (\text{A1})$$

For $w(\theta_i; \Theta)$ in equation (A1), we use the best-fitting linearly-biased dark matter model for the combined field obtained in section 4.3, $(b, f_{\text{fake}}) = (1.60, 0.140)$ for $z = 1.19$ and $(b, f_{\text{fake}}) = (2.08, 0.140)$ for $z = 1.47$. The red points show the result with the integral constraint correction, $\hat{w}_k + (1 - f_{\text{fake}})^2 w_{\Omega}$. For comparison, the measurement from all four fields with the integral constraint calculated using the same model is plotted as the blue dashed curve. One can see that the measurement from each field is largely consistent with each other. Thus, throughout this paper we perform the statistical analysis only for the data combined over all the four fields.

Appendix 2 Constraints on HOD parameters using clustering only

Given an HOD model for a certain galaxy population, the average number density is calculated by equation (21). One therefore needs to simultaneously analyze the observed correlation function and number density to constrain the HOD model, as

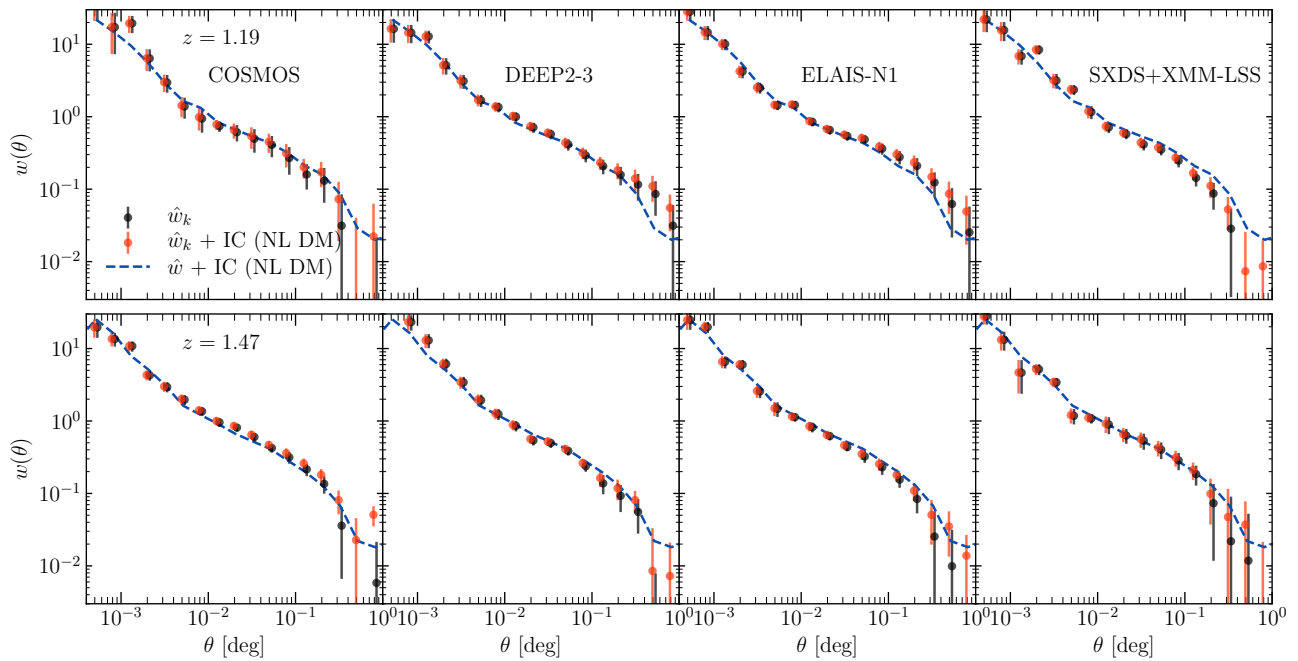


Fig. 13. Angular correlation functions of [OII] emitters of each of the four fields measured at $z = 1.19$ (top) and $z = 1.47$ (bottom). In each column, the measurement from each of the individual four fields is presented. The black points are the raw measurement without the correction of the integral constraints, \hat{w}_k ($1 \leq k \leq 4$). The red points are after the integral constraint (denoted by IC in the legend) is taken into account with the linearly-biased dark matter model, $\hat{w}_k + (1 - f_{\text{fake}})^2 w_{\Omega, k}$, with the best-fitting parameters obtained for the combined field, $(b, f_{\text{fake}}) = (1.60, 0.140)$ ($z = 1.19$) and $(b, f_{\text{fake}}) = (2.08, 0.140)$ ($z = 1.47$). For the reference, the angular correlation function measured for the combined field, $\hat{w} + (1 - f_{\text{fake}})^2 w_{\Omega}$, is shown as the blue dashed curve.

performed in section 5.3. In this appendix, we present the constraints on the HOD parameters based on Geach and Zheng models without using the information of the measured number density of [OII] emitters for readers who are interested in the constraining power coming from the clustering only (see, e.g., Matsuoka et al. 2011; Martinez-Manso et al. 2015 for a similar attempt).

Table 5 shows these results without using the abundance information. The halo mass parameters are strongly constrained by the abundance of [OII] emitters. The constraints on these parameters are thus not as tight as those presented in tables 3 and 4, as expected: the errors on M_c and M_{min} constraints without the abundance information in the Geach model are ~ 1.5 and ~ 3 times larger than those with the simultaneous analysis of clustering and abundance, and the errors on M_{min} and M_1 constraints without the abundance information in the Zheng model are ~ 3 and ~ 4 times larger. There are not significant changes in the constraints of the other HOD parameters. Interestingly, even though we do not use the number density to constrain the HOD parameters, the posterior of the number density is consistent with the observed one.

References

- Abbas, U., de la Torre, S., Le Fèvre, O., et al. 2010, MNRAS, 406, 1306
- Adams, J. J., Blanc, G. A., Hill, G. J., et al. 2011, ApJS, 192, 5
- Addison, G. E., Bennett, C. L., Jeong, D., Komatsu, E., & Weiland, J. L. 2019, ApJ, 879, 15
- Aihara, H., Armstrong, R., Bickerton, S., et al. 2018a, PASJ, 70, S8
- Aihara, H., Arimoto, N., Armstrong, R., et al. 2018b, PASJ, 70, S4
- Aihara, H., AlSayyad, Y., Ando, M., et al. 2019, PASJ, 71, 114
- Avila, S., Gonzalez-Perez, V., Mohammad, F. G., et al. 2020, MNRAS, 499, 5486
- Behroozi, P. S., Wechsler, R. H., & Conroy, C. 2013, ApJ, 770, 57
- Berlind, A. A., & Weinberg, D. H. 2002, ApJ, 575, 587
- Blake, C., Collister, A., & Lahav, O. 2008, MNRAS, 385, 1257
- Bocquet, S., & Carter, F. W. 2016, The Journal of Open Source Software, 1, doi:10.21105/joss.00046
- Bosch, J., Armstrong, R., Bickerton, S., et al. 2018, PASJ, 70, S5
- Bullock, J. S., Wechsler, R. H., & Somerville, R. S. 2002, MNRAS, 329, 246
- Cochrane, R. K., Best, P. N., Sobral, D., et al. 2018, MNRAS, 475, 3730
- . 2017, MNRAS, 469, 2913
- Comparat, J., Zhu, G., Gonzalez-Perez, V., et al. 2016, MNRAS, 461, 1076
- Conroy, C., Wechsler, R. H., & Kravtsov, A. V. 2006, ApJ, 647, 201
- Contreras, S., Baugh, C. M., Norberg, P., & Padilla, N. 2013, MNRAS, 432, 2717
- Cooray, A., & Sheth, R. 2002, Phys. Rep., 372, 1
- Coupon, J., Czakon, N., Bosch, J., et al. 2018, PASJ, 70, S7
- Coupon, J., Kilbinger, M., McCracken, H. J., et al. 2012, A&A, 542, A5
- Crocce, M., Cabré, A., & Gaztañaga, E. 2011, MNRAS, 414, 329
- Dawson, K. S., Kneib, J.-P., Percival, W. J., et al. 2016, AJ, 151, 44
- de la Torre, S., Guzzo, L., Peacock, J. A., et al. 2013, A&A, 557, A54

Table 5. Priors and constraints of the HOD parameters for Geach and Zheng models obtained using the clustering information only*

Geach HOD model			
Parameter	Prior	<i>NB816</i> Posterior PDF	<i>NB921</i> Posterior PDF
$\log M_c/(h^{-1}M_\odot)$	None	$11.50^{+0.72}_{-0.28}$	$11.70^{+0.25}_{-0.20}$
$\log M_{\min}/(h^{-1}M_\odot)$	None	$11.40^{+1.25}_{-1.00}$	$11.89^{+0.76}_{-1.36}$
$\sigma_{\log M}$	[0, 1]	$0.27^{+0.33}_{-0.17}$	$0.22^{+0.16}_{-0.13}$
α	1.00 ± 0.20	$0.96^{+0.11}_{-0.09}$	$1.10^{+0.13}_{-0.13}$
F_c^A	[0, 0.5]	$0.22^{+0.14}_{-0.07}$	$0.17^{+0.18}_{-0.06}$
F_c^B	[0, 1]	$0.56^{+0.32}_{-0.39}$	$0.61^{+0.27}_{-0.34}$
F_s	[0, 1]	$0.54^{+0.32}_{-0.30}$	$0.52^{+0.32}_{-0.34}$
f_{fake}	0.140 ± 0.060	$0.124^{+0.054}_{-0.051}$	$0.091^{+0.054}_{-0.046}$
Inferred quantity	Measurement	Posterior PDF	Posterior PDF
$\log n_g/(h^{-1}\text{Mpc})^{-3}$...	$-1.47^{+0.89}_{-0.80}$	$-1.96^{+1.18}_{-0.42}$
f_{sat}	...	$0.58^{+0.33}_{-0.43}$	$0.38^{+0.54}_{-0.23}$
b_{eff}	...	$1.64^{+0.12}_{-0.10}$	$1.94^{+0.13}_{-0.11}$
$\log M_{\text{eff}}/(h^{-1}M_\odot)$...	$12.70^{+0.10}_{-0.09}$	$12.63^{+0.12}_{-0.10}$
Zheng HOD model			
Parameter	Prior	<i>NB816</i> Posterior PDF	<i>NB921</i> Posterior PDF
$\log M_{\min}/(h^{-1}M_\odot)$	None	$12.01^{+0.62}_{-0.61}$	$11.85^{+0.56}_{-0.26}$
$\log M_1/(h^{-1}M_\odot)$	None	$12.97^{+0.43}_{-0.64}$	$12.91^{+0.36}_{-0.31}$
$\sigma_{\log M}$	[0, 1]	$0.58^{+0.30}_{-0.41}$	$0.32^{+0.41}_{-0.22}$
α	1.00 ± 0.20	$0.94^{+0.11}_{-0.11}$	$1.02^{+0.11}_{-0.11}$
f_{fake}	0.140 ± 0.060	$0.123^{+0.060}_{-0.063}$	$0.077^{+0.055}_{-0.047}$
Inferred quantity	Measurement	Posterior PDF	Posterior PDF
$\log n_g/(h^{-1}\text{Mpc})^{-3}$...	$-2.24^{+0.56}_{-0.44}$	$-2.27^{+0.28}_{-0.38}$
f_{sat}	...	$0.113^{+0.100}_{-0.044}$	$0.106^{+0.047}_{-0.040}$
b_{eff}	...	$1.64^{+0.15}_{-0.15}$	$1.91^{+0.13}_{-0.11}$
$\log M_{\text{eff}}/(h^{-1}M_\odot)$...	$12.633^{+0.102}_{-0.107}$	$12.534^{+0.091}_{-0.077}$

* In the ‘‘Prior’’ column the ranges specified in brackets are for uniform priors while the others we quote the mean and standard deviation of the Gaussian priors. In the column of ‘‘Posterior PDF’’, the central value is a median and the error means 16 – 84 percentiles after other parameters are marginalized over.

- DESI Collaboration, Aghamousa, A., Aguilar, J., et al. 2016, arXiv e-prints, arXiv:1611.00036
- Doré, O., Bock, J., Ashby, M., et al. 2014, arXiv e-prints, arXiv:1412.4872
- Duffy, A. R., Schaye, J., Kay, S. T., & Dalla Vecchia, C. 2008, MNRAS, 390, L64
- Durkalec, A., Le Fèvre, O., Pollo, A., et al. 2015, A&A, 583, A128
- Efstathiou, G., Bernstein, G., Katz, N., Tyson, J. A., & Guhathakurta, P. 1991, ApJL, 380, L47
- Favole, G., Comparat, J., Prada, F., et al. 2016, MNRAS, 461, 3421
- Favole, G., Gonzalez-Perez, V., Stoppacher, D., et al. 2020, MNRAS, 497, 5432
- Foreman-Mackey, D., Hogg, D. W., Lang, D., & Goodman, J. 2013, PASP, 125, 306
- Furusawa, H., Koike, M., Takata, T., et al. 2018, PASJ, 70, S3
- Gao, H., & Jing, Y. P. 2020, arXiv e-prints, arXiv:2007.12878
- Geach, J. E., Smail, I., Best, P. N., et al. 2008, MNRAS, 388, 1473
- Geach, J. E., Sobral, D., Hickox, R. C., et al. 2012, MNRAS, 426, 679
- Gonzalez-Perez, V., Comparat, J., Norberg, P., et al. 2018, MNRAS, 474, 4024
- Gonzalez-Perez, V., Cui, W., Contreras, S., et al. 2020, MNRAS, 498, 1852
- Guo, H., Zheng, Z., Zehavi, I., et al. 2014, MNRAS, 441, 2398
- Guo, H., Yang, X., Raichoor, A., et al. 2019, ApJ, 871, 147
- Hadzhiyska, B., Tacchella, S., Bose, S., & Eisenstein, D. J. 2020, arXiv e-prints, arXiv:2011.05331
- Hamana, T., Ouchi, M., Shimasaku, K., Kayo, I., & Suto, Y. 2004, MNRAS, 347, 813
- Harikane, Y., Ouchi, M., Ono, Y., et al. 2016, ApJ, 821, 123
- . 2018, PASJ, 70, S11
- Hartlap, J., Simon, P., & Schneider, P. 2007, A&A, 464, 399
- Hayashi, M., Sobral, D., Best, P. N., Smail, I., & Kodama, T. 2013, MNRAS, 430, 1042
- Hayashi, M., Ly, C., Shimasaku, K., et al. 2015, PASJ, 67, 80
- Hayashi, M., Tanaka, M., Shimakawa, R., et al. 2018, PASJ, 70, S17
- Hayashi, M., Shimakawa, R., Tanaka, M., et al. 2020, PASJ, 72, 86

- Hikage, C., Mandelbaum, R., Takada, M., & Spergel, D. N. 2013, *MNRAS*, 435, 2345
- Hong, S., Dey, A., Lee, K.-S., et al. 2019, *MNRAS*, 483, 3950
- Hsieh, B. C., & Yee, H. K. C. 2014, *ApJ*, 792, 102
- Huang, S., Leauthaud, A., Murata, R., et al. 2018, *PASJ*, 70, S6
- Ishikawa, S., Kashikawa, N., Toshikawa, J., et al. 2017, *ApJ*, 841, 8
- Ishikawa, S., Kashikawa, N., Tanaka, M., et al. 2020, *ApJ*, 904, 128
- Jing, Y. P., Mo, H. J., & Boerner, G. 1998, *ApJ*, 494, 1
- Kaiser, N. 1984, *ApJL*, 284, L9
- Kashino, D., More, S., Silverman, J. D., et al. 2017, *ApJ*, 843, 138
- Kayo, I., & Oguri, M. 2012, *MNRAS*, 424, 1363
- Khostovan, A. A., Sobral, D., Mobasher, B., et al. 2018, *MNRAS*, 478, 2999
- Kim, H.-S., Baugh, C. M., Benson, A. J., et al. 2011, *MNRAS*, 414, 2367
- Koda, J., Blake, C., Beutler, F., Kazin, E., & Marin, F. 2016, *MNRAS*, 459, 2118
- Komiyama, Y., Obuchi, Y., Nakaya, H., et al. 2018, *PASJ*, 70, S2
- Landy, S. D., & Szalay, A. S. 1993, *ApJ*, 412, 64
- Laureijs, R., Amiaux, J., Arduini, S., et al. 2011, *arXiv e-prints*, arXiv:1110.3193
- Leung, A. S., Acquaviva, V., Gawiser, E., et al. 2017, *ApJ*, 843, 130
- Limber, D. N. 1954, *ApJ*, 119, 655
- Lupton, R. 1993, *Statistics in theory and practice*
- Ly, C., Malkan, M. A., Kashikawa, N., et al. 2012, *ApJ*, 757, 63
- Ma, C.-P., & Fry, J. N. 2000, *ApJ*, 543, 503
- Martinez-Manso, J., Gonzalez, A. H., Ashby, M. L. N., et al. 2015, *MNRAS*, 446, 169
- Matsuoka, Y., Masaki, S., Kawara, K., & Sugiyama, N. 2011, *MNRAS*, 410, 548
- Miyazaki, S., Komiyama, Y., Nakaya, H., et al. 2012, in *Proc. SPIE*, Vol. 8446, *Ground-based and Airborne Instrumentation for Astronomy IV*, 84460Z
- Miyazaki, S., Komiyama, Y., Kawanomoto, S., et al. 2018, *PASJ*, 70, S1
- Moustakas, L. A., & Somerville, R. S. 2002, *ApJ*, 577, 1
- Murray, S. G., Power, C., & Robotham, A. S. G. 2013, *Astronomy and Computing*, 3, 23
- Navarro, J. F., Frenk, C. S., & White, S. D. M. 1997, *ApJ*, 490, 493
- Oguri, M., & Lin, Y.-T. 2015, *ApJ*, 801, 94
- Okada, H., Totani, T., Tonegawa, M., et al. 2016, *PASJ*, 68, 47
- Okumura, T., Hand, N., Seljak, U., Vlah, Z., & Desjacques, V. 2015, *Phys. Rev. D*, 92, 103516
- Okumura, T., Takada, M., More, S., & Masaki, S. 2017, *MNRAS*, 469, 459
- Okumura, T., Hikage, C., Totani, T., et al. 2016, *PASJ*, 68, 38
- Osato, K., & Okumura, T. 2021, in prep.
- Peacock, J. A., & Smith, R. E. 2000, *MNRAS*, 318, 1144
- Peebles, P. J. E. 1973, *ApJ*, 185, 413
- . 1980, *The large-scale structure of the universe* (Princeton, N.J., Princeton Univ. Press)
- Peebles, P. J. E., & Groth, E. J. 1976, *A&A*, 53, 131
- Planck Collaboration, Ade, P. A. R., Aghanim, N., et al. 2016, *A&A*, 594, A13
- Reid, B. A., Seo, H.-J., Leauthaud, A., Tinker, J. L., & White, M. 2014, *MNRAS*, 444, 476
- Richardson, J., Zheng, Z., Chatterjee, S., Nagai, D., & Shen, Y. 2012, *ApJ*, 755, 30
- Saito, S., de la Torre, S., Ilbert, O., et al. 2020, *MNRAS*, 494, 199
- Saito, S., Leauthaud, A., Hearin, A. P., et al. 2016, *MNRAS*, 460, 1457
- Scoccimarro, R., Sheth, R. K., Hui, L., & Jain, B. 2001, *ApJ*, 546, 20
- Seljak, U. 2000, *MNRAS*, 318, 203
- Simon, P. 2007, *A&A*, 473, 711
- Takada, M., Ellis, R. S., Chiba, M., et al. 2014, *PASJ*, 66, 1
- Takahashi, R., Sato, M., Nishimichi, T., Taruya, A., & Oguri, M. 2012, *ApJ*, 761, 152
- Tinker, J. L., Robertson, B. E., Kravtsov, A. V., et al. 2010, *ApJ*, 724, 878
- Tonegawa, M., Totani, T., Okada, H., et al. 2015, *PASJ*, 67, 81
- Totsuji, H., & Kihara, T. 1969, *PASJ*, 21, 221
- van den Bosch, F. C., More, S., Cacciato, M., Mo, H., & Yang, X. 2013, *MNRAS*, 430, 725
- Wake, D. A., Whitaker, K. E., Labbé, I., et al. 2011, *ApJ*, 728, 46
- Weinberg, D. H., Mortonson, M. J., Eisenstein, D. J., et al. 2013, *Phys. Rep.*, 530, 87
- White, M., Blanton, M., Bolton, A., et al. 2011, *ApJ*, 728, 126
- Zehavi, I., Eisenstein, D. J., Nichol, R. C., et al. 2005, *ApJ*, 621, 22
- Zehavi, I., Zheng, Z., Weinberg, D. H., et al. 2011, *ApJ*, 736, 59
- Zheng, Z., Coil, A. L., & Zehavi, I. 2007, *ApJ*, 667, 760
- Zheng, Z., Zehavi, I., Eisenstein, D. J., Weinberg, D. H., & Jing, Y. P. 2009, *ApJ*, 707, 554
- Zheng, Z., Berlind, A. A., Weinberg, D. H., et al. 2005, *ApJ*, 633, 791